Instability and dynamics of volatile thin films

Hangjie Ji*
Department of Mathematics, University of California, Los Angeles, Los Angeles, California 90095, USA

Thomas P. Witelski†
Department of Mathematics, Duke University, Durham, North Carolina 27708-0320, USA

(Received 31 August 2017; published 1 February 2018)

Volatile viscous fluids on partially wetting solid substrates can exhibit interesting interfacial instabilities and pattern formation. We study the dynamics of vapor condensation and fluid evaporation governed by a one-sided model in a low-Reynolds-number lubrication approximation incorporating surface tension, intermolecular effects, and evaporative fluxes. Parameter ranges for evaporation-dominated and condensation-dominated regimes and a critical case are identified. Interfacial instabilities driven by the competition between the disjoining pressure and evaporative effects are studied via linear stability analysis. Transient pattern formation in nearly flat evolving films in the critical case is investigated. In the weak evaporation limit unstable modes of finite-amplitude nonuniform steady states lead to rich droplet dynamics, including flattening, symmetry breaking, and droplet merging. Numerical simulations show that long-time behaviors leading to evaporation or condensation are sensitive to transitions between filmwise and dropwise dynamics.

DOI: 10.1103/PhysRevFluids.3.024001

I. INTRODUCTION

Pattern formation of thin liquid films has been studied in many experimental and theoretical works [1,2] and has important connections to many engineering applications of coating flows. Morphological changes such as localized thinning, rupture, coarsening, and droplet dynamics can arise from instabilities caused by the interaction of various physical influences. In the limit of low Reynolds number, the governing Navier Stokes equations can be reduced to a thin-film equation for the evolution of the thickness of the fluid layer on a solid substrate. Lubrication models for free-surface flows of these thin layers of viscous fluids have been studied extensively in many contexts [3–6].

In this work we will take a closer look at a thin-film model for a volatile viscous fluid on a solid at a fixed temperature, where the temperature difference with the surrounding vapor can drive evaporation or condensation. Specifically, the aim of this paper is to understand the forms of dynamics that can result from the interaction of substrate wettability and evaporation or condensation of the fluid. Stability analysis will show that both significant transient dynamics and a strong dependence on initial conditions can occur as the fluid layer evolves between droplike and filmlike states.

Wetting properties of solid substrates can qualitatively affect the behavior of ultrathin layers (less than 100 nm) of fluids. While hydrophilic or wetting materials encourage the spreading of fluids to form more uniform films, hydrophobic or nonwetting solids repel the fluid and favor breakup into structures that ultimately leads to arrays of droplets [7–9]. Generally called dewetting phenomena, these interactions are driven by van der Waals forces between the solid and fluid and are modeled

*hangjie@math.ucla.edu
†witelski@math.duke.edu

by a disjoining pressure as a contribution to the dynamic pressure in the thin-film equation. Early stages of the dynamics involve instabilities of flat films [10] leading to finite-time rupture [11,12] and later growth of dry spots [8,9,13–15] and coarsening dynamics of interacting metastable droplets [16]. These studies have addressed how spatial structures in the films develop subject to the overall conservation of mass for nonvolatile fluids. There has been less work on how the change of mass from slow evaporation or condensation interacts with dewetting behavior [13,17,18].

The study of thin films subject to fluid evaporation and vapor condensation is especially important for systems such as precorneal tear films [19], thermal management [20], and drying paint layers [21,22]. In particular, since dropwise condensation on hydrophobic surfaces is more energy efficient compared to the filmwise condensation mode [23], many studies have considered the influence of the surface wettability on the dynamics [24–27].

The basic physics of thin films with phase changes has many applications in many systems in engineering and other physical systems [28]. Describing the evaporative mass flux across the liquid-vapor interface generally involves the influence of both the liquid phase and the diffusion of the vapor, as in the two-sided model in [29]. Simplified one-sided models are obtained by decoupling the dynamics of the fluid from that of the spatially uniform vapor concentration. Burelbach *et al.* [30] proposed a one-sided model by assuming that the density, viscosity, and thermal conductivity in the vapor are negligible compared to those in the liquid. Following their work, Oron and Bankoff [31,32] investigated the dynamics of a condensing thin liquid film using an evaporative mass flux only dependent on film thickness and neglected effects such as thermocapillarity and vapor thrust. A model was derived by Ajaev and Homsy [33–35] that incorporates thermal effects, surface tension, and disjoining pressure in the evaporative flux. In all of these models the dynamics of the vapor phase are not included except through a boundary condition at the vapor-fluid interface. Related problems of evaporating liquid droplets associated with moving contact lines were also studied [33,36,37]. For a thorough review of the modeling and numerical studies of volatile thin films, see [3,38].

While some results are available for the stability and dynamics of volatile polar thin films on partially wettable solid substrates with various forms of evaporative fluxes [33,34,39,40], the nonlinear stability and pattern formation of thin films undergoing phase change on a hydrophobic substrate still need further investigation. The competition between the evaporation or condensation effects and the disjoining pressure is the focus of our paper. We will show that interfacial instabilities driven by the disjoining pressure can yield transient pattern formation under weak evaporation. Balances between the evaporative effects, intermolecular forces, and the surface tension produce a family of spatially uniform or periodic steady states whose instabilities lead to interesting transitions between dropwise and filmwise dynamics.

The structure of this paper is as follows. In Sec. II the model for volatile thin films on a partially wetting substrate is formulated. In Sec. III spatially uniform states will be discussed and the related transient instabilities with respect to spatial perturbations will be investigated via linear stability analysis. Spatially periodic steady states representing droplets will be presented in Sec. IV and their stability will be analyzed in Sec. V. Numerical simulations of the model and comparison with the analytical predictions for systems with small numbers of droplets are given in Sec. VI. A discussion of remaining open questions is given in Sec. VII.

II. MODEL FORMULATION

We consider a two-dimensional thin fluid film spreading over a uniformly heated or cooled solid substrate (shown in Fig. 1). Under the long-wavelength approximation and in the limit of the low Reynolds number, the classic thin-film equation can be derived from the full Navier-Stokes equations [6]. Following [35], we consider an evaporating-condensing thin-film equation by including an additional flux term to a mass-conserving thin-film model.

We consider a Newtonian fluid with density ρ, viscosity μ, thermal conductivity κ, and specific latent heat $\mathcal{L}$. The dimensional scales for the model are chosen following [33–35]. If the lateral length scale is L_x, then the characteristic velocity is $U = \kappa T^*/\rho\mathcal{L}L_x$, set by a mass balance at

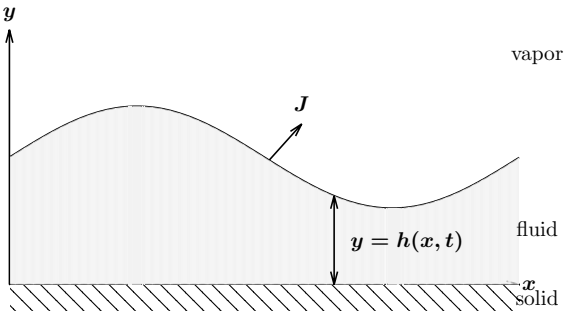

FIG. 1. Schematic representation of a two-dimensional thin fluid film on a uniformly heated (cooled) solid substrate where J represents the evaporative (condensing) mass flux.

the free surface with T^* being the liquid saturation temperature. The capillary number is given by $C = \mu U/\sigma$ and the pressure and time scales are given by $\sigma C^{1/3}/L_x$ and $3L_x/U$, respectively, where σ is the surface tension. We will consider small temperature differences from T^* and will argue that variations to σ can be neglected.

The resulting governing equation in nondimensional form for viscous coating flows is given by a one-dimensional fourth-order nonlinear partial differential equation for the thickness h of the fluid layer over a periodic domain on $0 \leqslant x \leqslant L$,

$$\frac{\partial h}{\partial t} = \frac{\partial}{\partial x}\left(h^3 \frac{\partial p}{\partial x}\right) - J, \tag{1a}$$

where the evaporative mass flux is given by

$$J(h) = \frac{\beta p(h)}{h + K_0}, \tag{1b}$$

with the hydrodynamic pressure $p(h)$ incorporating the influences of kinetics at the interface [34], surface tension [4], and wetting properties of the substrate. The dimensionless parameters are given by

$$\beta = \frac{3\sigma}{\rho \mathcal{L} C^{1/3} L_x}, \quad K_0 = \frac{\rho U \sqrt{2\pi \bar{R} T^*}}{2\rho_v \mathcal{L} C^{1/3}}, \tag{1c}$$

arising from a thermodynamic-kinetic condition at the interface [33], which relates the jump in both temperature and pressure at the fluid-vapor interface to the evaporative mass flux. The parameter β scales the effect of changes in the dynamic pressure in the evaporation and condensation effects and the parameter K_0 characterizes the importance of phase-change kinetics at the interface [35]. Here $\bar{R}$ is the gas constant per unit mass and ρ_v is the vapor density. The pressure in (1b) is given by the difference between a generalized disjoining pressure $\Pi(h)$ and the linearized curvature of the interface

$$p(h) = \Pi(h) - \frac{\partial^2 h}{\partial x^2}, \tag{1d}$$

where $\Pi(h)$ is shifted by a constant P_0 from a standard disjoining pressure $\tilde{\Pi}(h)$ describing substrate wetting properties,

$$\Pi(h) = \tilde{\Pi}(h) - P_0 \quad \text{with } \tilde{\Pi}(h) = \frac{A}{h^3}\left(1 - \frac{\epsilon}{h}\right) \tag{1e}$$

and

$$P_0 = -\frac{T_0 - T^*}{\beta C^{2/3} T^*}, \tag{1f}$$

where T_0 is the temperature at the fluid-solid interface.

The product of β and P_0 in the evaporative flux (1b) represents the scaled difference of the temperature of the heated or cooled solid substrate from the liquid saturation temperature. Specifically, $P_0 < 0$ indicates that the vapor phase is undersaturated and $P_0 > 0$ corresponds to supersaturated vapor. Note that adding a constant to the disjoining pressure $\Pi(h)$ will not change the form of the conservative flux since it is given by the gradient of the pressure in the partial differential equation (PDE) (1a). With this form, $\Pi(h) = \tilde{\Pi}(h) - P_0$, the pressure term in the evaporative flux (1b) is consistent with that in the conservative term.

In the present work we use the physically motivated regularized form of $\tilde{\Pi}(h)$ in (1e) with the rescaled Hamaker constant A. We will use $A > 0$ in $\tilde{\Pi}(h)$ to indicate the overall hydrophobic character of the substrate. The dimensionless parameter $\epsilon > 0$ is set by the height at which the attractive van der Waals forces and short-range Born repulsion balance and provide a positive $O(\epsilon)$ lower bound for the film thickness [22,31,32,41]. For the rest of the paper, we will use the scaling $A = \epsilon^2$, following other studies of dewetting films [6,31,41].

Different forms of $\tilde{\Pi}(h)$ have been used in the literature to characterize the hydrophobic or hydrophilic properties of the substrate. For instance, the form $\tilde{\Pi}(h) = A/h^3$ represents [42] unbalanced van der Waals forces. It has been shown [10] that instabilities caused by this form of $\tilde{\Pi}(h)$ with $A > 0$ can lead to finite-time rupture, that is, the film thickness h approaches zero at an isolated point as a critical time is approached [11,12]. For the case $A < 0$ this $\tilde{\Pi}(h)$ can describe the wetting property of a hydrophilic substrate [17,35].

Several other forms of evaporation loss or condensation source terms have also been used in the literature. In [30,37,43] a simple form for the evaporative mass flux term is taken, $J(h) = E_0/(h + K_0)$, where the dimensionless evaporation number E_0 distinguishes the evaporation case with $E_0 > 0$ from the condensation case with $E_0 < 0$. In the evaporation model for a thin film on a wetting substrate derived by Ajaev and Homsy [33–35] the evaporative flux takes the form in (1b) with $\tilde{\Pi} = A/h^3$ for $A < 0$. In [40,44] a different form of the evaporative flux was derived by assuming that the flux is proportional to the difference between the chemical potential of the vapor and the liquid.

An important implication of the form of the evaporative flux (1b) is that the local condensation or evaporation depends on three factors: the film thickness, the surface tension, and the pressure P_0. For example, evaporation may occur from negatively curved portions of the film ($h_{xx} < 0$) even when the vapor is oversaturated with $P_0 > 0$, and a positively curved portion of the film ($h_{xx} > 0$) may condense when a negative P_0 is present if the curvature is large enough. This was also described in [28,40].

Thermal Marangoni stresses are generated by variations in the surface tension due to its dependence on temperature. Papers that consider thermocapillary stresses driven by large temperature gradients include [30,34,43]. In this paper we focus on dynamics subject to small temperature differences from the saturation temperature T^* and small length scale [35,45]; under these conditions we make the assumption that Marangoni stresses are weak and can be omitted from (1a). Other papers on volatile thin films that show that thermocapillary stresses can be neglected under appropriate conditions include [17,46,47].

Starting from positive and finite-mass initial data $h_0(x) > 0$ at time $t = 0$, the dynamics of the model (1) is governed by the interactions between the mass-conserving spatial flux and the evaporative flux. It is convenient to write the generalized potential as the integral of $\Pi(h)$,

$$U(h) = \int \Pi(h) dh = -\frac{\epsilon^2}{2h^2} + \frac{\epsilon^3}{3h^3} - P_0 h. \tag{2}$$

This form combines the intermolecular forces between the fluid and the solid substrate, and the evaporation and condensation effects through the last term. Following results from [18], we define the energy functional that governs the dynamics of (1) as

$$\mathcal{E}[h] = \int_0^L \frac{1}{2}\left(\frac{\partial h}{\partial x}\right)^2 + U(h)dx. \tag{3}$$

A direct calculation of the time derivative of the functional (3) leads to the dissipation of energy

$$\frac{d\mathcal{E}}{dt} = -\left[\int_0^L h^3\left(\frac{\partial p}{\partial x}\right)^2 dx + \beta\int_0^L \frac{p^2}{h+K_0}dx\right] \leqslant 0. \tag{4}$$

This observation will be used for a short proof that evaporation can never overcome the disjoining pressure in the Appendix; this behavior is physically expected for adsorbed films, but is not guaranteed for all mathematical forms of evaporative fluxes [48].

Since the contribution from each integral in (4) is non-negative, at an equilibrium state each integral must equal zero independently. The first integral yields that $\partial p/\partial x = 0$, which indicates that p is a constant over the domain. For $\beta > 0$ the second integral in (4) being zero then leads to $p \equiv 0$. Whether equilibria exist as drops or uniform films depends on the pressure offset P_0; our analysis of the dynamics will be partitioned into regimes determined by the equilibrium solutions.

The total mass of the film is of key interest and its rate of change due to the evaporative term can be obtained by integrating Eq. (1a) and incorporating the periodic boundary conditions

$$\mathcal{M}(t) = \int_0^L h\,dx, \quad \frac{d\mathcal{M}}{dt} = -\beta\int_0^L \frac{p}{h+K_0}dx. \tag{5}$$

Using (1d) and performing an integration by parts, we get

$$\frac{d\mathcal{M}}{dt} = \beta\left(\int_0^L \frac{h_x^2}{(h+K_0)^2}dx - \int_0^L \frac{\Pi(h)}{h+K_0}dx\right). \tag{6}$$

For the special case with $\beta = 0$ the mass is conserved and no evaporation or condensation occurs. In other cases, the increase or decrease of the mass is more complicated. For $\beta > 0$, this indicates that if $\Pi(h) \leqslant 0$ over the domain, then (6) yields a positive growth rate, namely, condensation, while if $\Pi(h)$ is sufficiently large to overcome the first integral, then evaporation occurs. In the critical case where the sign of $\Pi(h)$ is changeable, transitions between condensation and evaporation can occur.

To study the interesting combination of dewetting and evaporative and condensing effects, we will start exploring by examining the instability of both spatially uniform and nonuniform equilibrium solutions.

III. STABILITY OF SPATIALLY UNIFORM FILMS

We begin by examining the dynamics for solutions that are perturbations of uniform flat fluid layers. Since mass is not conserved, the mean height $\bar{h}(t)$ can evolve with time and there is a need to cover a range of behaviors spanning from evaporating down to uniform adsorbed layers to flooding under condensation.

We follow the approach in [40,48] and perturb the uniform film by an infinitesimal Fourier mode disturbance

$$h(x,t) \sim \bar{h}(t) + \delta e^{i2k\pi x/L}e^{\sigma(t)}, \tag{7}$$

where k is the wave number and $\sigma(t)$ describes the growth of the perturbation starting from the initial amplitude $\delta \ll 1$, with $\sigma(0) = 0$. Expanding the PDE (1) about $h = \bar{h}$ then gives the $O(1)$ and $O(\delta)$

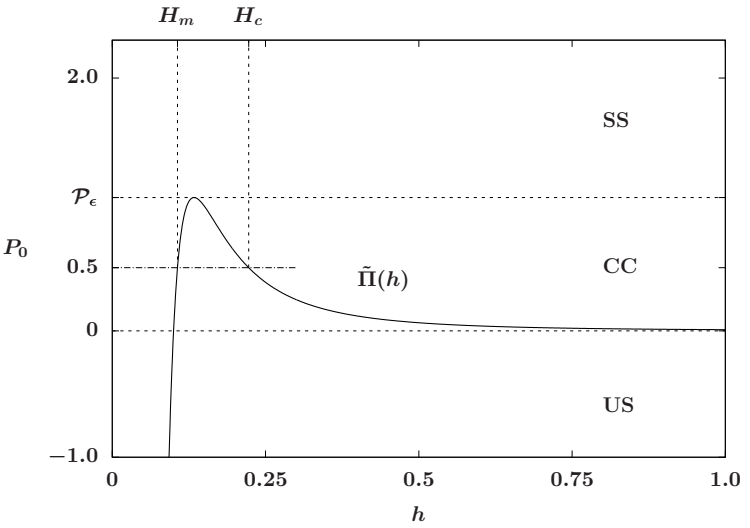

FIG. 2. Plot of $\tilde{\Pi}(h)$ given by (1e) with $\epsilon = 0.1$, with the dashed lines representing the thresholds of the parameter P_0, which determines the multiplicity of spatially uniform solutions in the system. The thresholds separate the undersaturated, critical case, and supersaturated regimes.

equations, respectively,

$$\frac{d\bar{h}}{dt} = -\beta \tilde{J}(\bar{h}) \quad \text{where } \tilde{J}(\bar{h}) = \frac{\Pi(\bar{h})}{\bar{h} + K_0}, \tag{8a}$$

$$\frac{d\sigma}{dt} = -\left[\left(\frac{2k\pi}{L}\right)^2 \bar{h}^3 + \frac{\beta}{\bar{h} + K_0}\right]\left[\Pi'(\bar{h}) + \left(\frac{2k\pi}{L}\right)^2\right] + \frac{\beta}{\bar{h} + K_0}\tilde{J}(\bar{h}), \tag{8b}$$

For $\beta \neq 0$, the equilibria of (8a) are the spatially uniform steady states of (1), namely, the heights yielding zero disjoining pressure $\Pi(\bar{h}) = 0$. As shown in Fig. 2, the number of spatially uniform steady states depends on the value of the parameter P_0 relative to the critical pressure $\mathcal{P}_\epsilon$ set by the disjoining pressure, from the unique maximum at $h_{\text{peak}} = \frac{4}{3}\epsilon$ where

$$\Pi(h_{\text{peak}}) = \mathcal{P}_\epsilon - P_0, \quad \mathcal{P}_\epsilon = \frac{27}{256}\epsilon^{-1} > 0. \tag{9}$$

In particular, there are three regimes.

(i) Undersaturated vapor (US). If $P_0 < 0$, there is one uniform steady state with $H_m < h_{\text{peak}}$.

(ii) Critical case (CC). If $0 < P_0 \leqslant \mathcal{P}_\epsilon$, there are two uniform steady states with $H_m \leqslant h_{\text{peak}} \leqslant H_c$.

(iii) Supersaturated vapor (SS). If $P_0 > \mathcal{P}_\epsilon$, there is no uniform steady state.

These cases for the range of P_0 are of central importance for both the stability analysis and dynamics of this problem. For $P_0 < \mathcal{P}_\epsilon$ in the critical and undersaturated cases, the spatially uniform steady state H_m defines a minimum thickness adsorbed layer,

$$H_m = \epsilon + P_0\epsilon^2 + 4P_0^2\epsilon^3 + O(\epsilon^4), \quad \epsilon \to 0, \tag{10}$$

while in the critical case, for $0 < P_0 < \mathcal{P}_\epsilon$, another constant steady state H_c also exists,

$$H_c = P_0^{-1/3}\epsilon^{2/3} - \tfrac{1}{3}\epsilon - \tfrac{2}{9}P_0^{1/3}\epsilon^{4/3} + O(\epsilon^{5/3}). \tag{11}$$

While H_c depends on P_0 in the leading order, H_m has a weaker dependence on P_0 with a saddle-node bifurcation occurring at $P_0 = \mathcal{P}_\epsilon$. Similar results on flat-film steady states are available in [39,40],

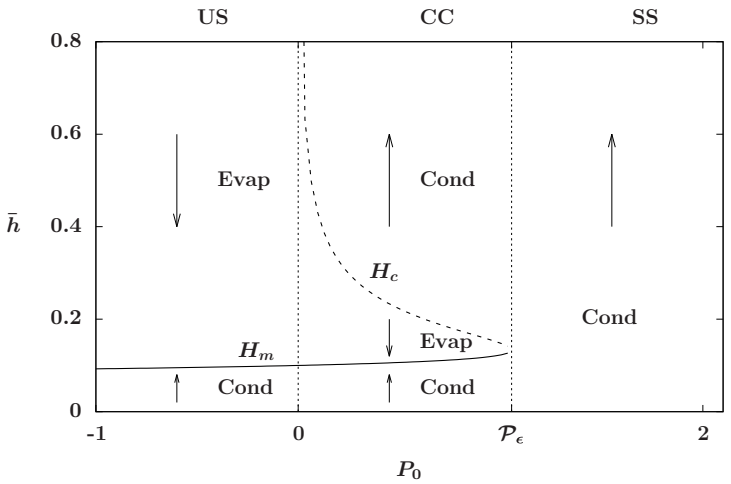

FIG. 3. Bifurcation diagram of the uniform steady states H_c and H_m as functions of P_0. Arrows indicate the dynamics for the mean thickness $\bar{h}(t)$ in each of the regimes US, CC, and SS: condensation with $\bar{h}(t)$ increasing or evaporation with $\bar{h}(t)$ decreasing, and H_m being stable while H_c is an unstable steady state.

where other forms for the disjoining pressure were used. For the rest of this article, we set the system parameters $\epsilon = K_0 = 0.1$, yielding $\mathcal{P}_\epsilon \approx 1.05$.

The equilibria H_m and H_c are fixed points of (8a) and then (8b) reduces to the dispersion relation for the growth rate of perturbations λ from standard linear stability analysis,

$$\sigma(t) = \lambda t, \quad \lambda(\bar{h}) = -\left[\left(\frac{2k\pi}{L}\right)^2 \bar{h}^3 + \frac{\beta}{\bar{h}+K_0}\right]\left[\Pi'(\bar{h}) + \left(\frac{2k\pi}{L}\right)^2\right]. \tag{12}$$

For $\bar{h} = H_m$, $\Pi'(\bar{h}) > 0$ to yield that $\lambda \leqslant 0$, so H_m is stable with respect to all perturbations. For $\bar{h} = H_c$, $\Pi'(\bar{h}) < 0$ and the thickness H_c is long-wave unstable with respect to perturbations with $0 \leqslant k < k_c$ below a critical wave number $k_c = L|\Pi'(H_c)|^{1/2}/2\pi$.

Linear stability analysis of films with other thicknesses has been previously carried out using the frozen time (or quasisteady $\bar{h}$) approach [30,39,49], but this is limited to only short-time behaviors. We will consider the evolution more globally by using the full dynamics of (8a) and (8b) for the mean film thickness and amplitude of spatial perturbations.

The loss or gain of mass and evolution of the mean film thickness $\bar{h}(t)$ follows directly from (8a) and the ranges of h for which $\Pi(h)$ is positive or negative (see Fig. 3). For the critical and undersaturated cases, the local linear stability and instability of H_m and H_c extend to show those states to be dividing lines between regimes of condensation and evaporation for uniform films. For the supersaturated case, $\Pi > 0$ for all $\bar{h} > 0$ and hence all films will exhibit condensation.

We now turn to (8b) to investigate the possibility for development of spatial patterns on the film surface. Figure 4(a) shows the growth rate $d\sigma/dt$ as a function of $\bar{h}$ for several values of P_0 at a given perturbation wave number $k = 6$. We observe that there exists a threshold pressure $P_0 = P_c(k)$ for the growth of spatial perturbations. For $P_0 < P_c$, films of thickness $\bar{h}$ are linearly unstable to perturbations over a band of average film thicknesses

$$\bar{h}_-(P_0,k) < \bar{h} < \bar{h}_+(P_0,k), \tag{13}$$

for which $d\sigma/dt > 0$ [see Fig. 4(b)]. To see an illustration of the impact of this instability, we consider an example with $P_0 = 0.5$ and the initial condition $h_0(x) = 0.2 + 10^{-4}\cos(12\pi x/L)$ in (1). Here the initial mean thickness is $\bar{h}_0 = 0.2$, which lies in the unstable range $\bar{h}_- < \bar{h} < \bar{h}_+$ for $k = 6$ [see Fig. 4(b)]. The value of $\bar{h}_0$ is also less than $H_c(P_0) \approx 0.222$, so by (8a) we expect evaporation to

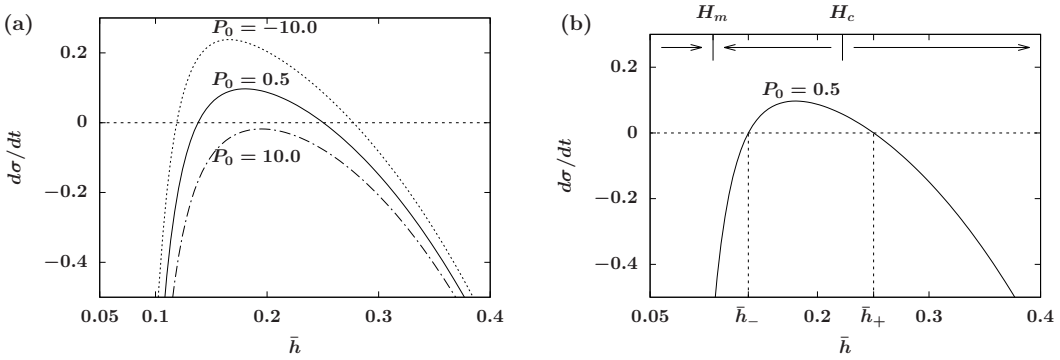

FIG. 4. (a) Plot of $d\sigma/dt$ vs $\bar{h}$ at several values of P_0 (with $k = 6$, $\beta = 0.001$, and $L = 20$ fixed). Here $P_c \approx 8.455$ is a threshold for growth of spatial instabilities for $P_0 < P_c$. (b) Critical film heights $\bar{h}_-, \bar{h}_+$ marking the range where spatial perturbations grow for $P_0 = 0.5$. This range of heights is different than the ranges for evaporation or condensation of uniform films set by the equilibria H_m, H_c.

occur. To compare the linearized model against direct simulations of (1), we define the average film thickness

$$\langle h \rangle = \frac{1}{L} \int_0^L h \, dx. \tag{14}$$

The simulation in Fig. 5(a) shows transient pattern formation with the perturbation amplitude growing while $\bar{h}(t)$ evolves downward through the unstable range. As $\bar{h}(t)$ crosses $\bar{h}_-$ the perturbations decay as the solution eventually converges to the spatially uniform steady state H_m. In Fig. 5(b) we compare the prediction for the evaporation rate from (8a) against the effective rate exhibited by the average thickness $d\langle h \rangle/dt \approx -\beta \tilde{J}(\langle h \rangle)$. We observe that for this example the assumptions in (8a) and (8b) hold well over most of the dynamics except for an intermediate period. When $\langle h \rangle \approx 0.13$ the spatial perturbations became sufficiently large to have nonlinear effects making deviations between $\bar{h}$ and $\langle h \rangle$ noticeable (with the nonlinear spatial perturbations having nonzero means).

To understand when the influences of transients will be significant, we examine the behavior described by (8b). Since we know that $\bar{h}$ evolves monotonically between the equilibria H_c and H_m, it is helpful to combine (8a) and (8b) to form the associated ordinary differential equation (ODE) for

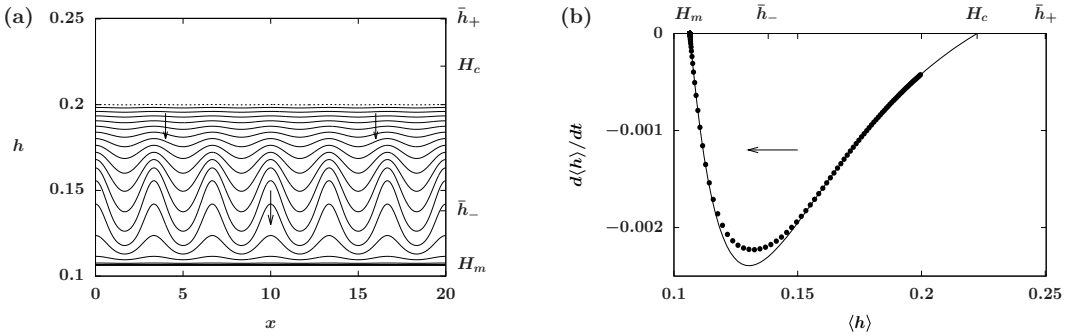

FIG. 5. (a) Evaporation with transient pattern formation starting from the initial data $h_0(x) = 0.2 + 10^{-4}\cos(12\pi x/L)$ with the system parameters $P_0 = 0.5$, $\beta = 0.001$, and $L = 20$. (b) Dots represent the effective rate of evaporation $d\langle h \rangle/dt$ plotted against the decreasing average film thickness in the PDE simulation, compared against the prediction $-\beta \tilde{J}(\langle h \rangle)$ from (8a) (solid curve).

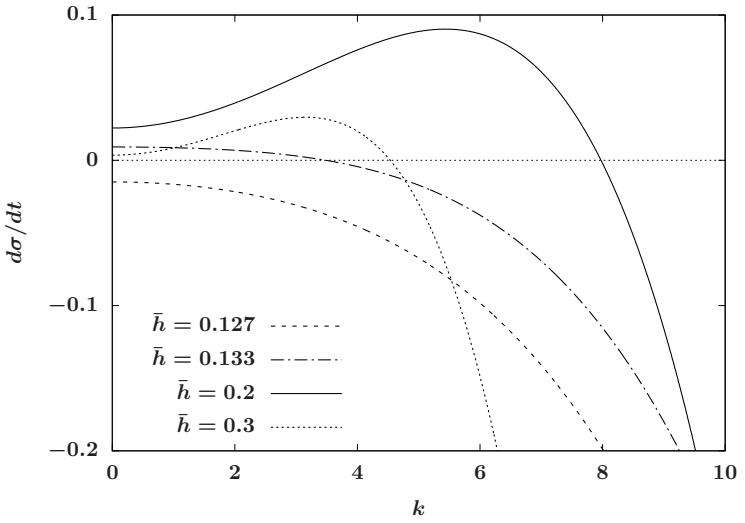

FIG. 6. Dispersion relation plot of $d\sigma/dt$ against the wave number k at the values $\bar{h} = 0.127, 0.133, 0.2, 0.3$. The parameter $P_0 = 0.5$ is in the critical case range $0 < P_0 < \mathcal{P}_\epsilon$ and the other parameters are identical to those in Fig. 4.

the evolution of the spatial perturbation amplitude with respect to changes in the mean thickness,

$$\frac{d\sigma}{d\bar{h}} = \frac{1}{\tilde{J}}\left[\frac{1}{\beta}\left(\frac{2k\pi}{L}\right)^2 \bar{h}^3 + \frac{1}{\bar{h}+K_0}\right]\left[\Pi'(\bar{h}) + \left(\frac{2k\pi}{L}\right)^2\right] - \frac{1}{\bar{h}+K_0}. \tag{15}$$

In the limit of weak evaporation and condensation effects, this takes the form

$$\frac{d\sigma}{d\bar{h}} \sim \frac{\bar{h}+K_0}{\beta\Pi(h)}\left(\frac{2k\pi}{L}\right)^2 \bar{h}^3\left[\Pi'(\bar{h}) + \left(\frac{2k\pi}{L}\right)^2\right] = O\left(\frac{1}{\beta}\right) \quad \text{for } \beta \to 0 \tag{16}$$

and hence we can conclude that for $\beta \to 0$ spatial perturbations can display large transient growth relative to given changes of the mean film height. Since the factor in square brackets in (16) is the same as in (12), we see that these transient instabilities share the same critical wave number k_c for long-wave instability. In general, the limit of weak phase-change effects ($\beta \to 0$) is a singular perturbation: For finite times (1) with $\beta \to 0$ approaches nonvolatile behavior, but for sufficiently long times ($t \to \infty$) changes in mass will create significant differences in behaviors.

In contrast, when β is large,

$$\frac{d\sigma}{d\bar{h}} \sim \frac{1}{\Pi(\bar{h})}\left[\Pi'(\bar{h}) + \left(\frac{2k\pi}{L}\right)^2\right] - \frac{1}{\bar{h}+K_0} = O(1) \quad \text{for } \beta \to \infty \tag{17}$$

and there is no separation of time scales between the evolution of $\bar{h}(t)$ and $\sigma(t)$. This means that with strong evaporation, perturbations would not have a chance to appreciably grow in amplitude before $\bar{h}(t)$ has moved out of the unstable range and hence rapidly evaporating films would always stay close to uniform in height.

Figure 6 gives the dispersion relation (8b) for several values of $\bar{h}$. We observe that for a range of $\bar{h}$ values the most unstable wave number is positive, $k^* > 0$. This means that patterns can develop for those thicknesses (see the $\bar{h} = 0.2$ and $\bar{h} = 0.3$ curves). Below some threshold for $\bar{h}$, the most unstable wave number is attained at $k^* = 0$, indicating that any spatial perturbations will decay relative to the evolution of the uniform film $\bar{h}(t)$ (see the $\bar{h} = 0.127$ and $\bar{h} = 0.133$ curves). For zero wave number these perturbations are constant in space, $\bar{h} \to \bar{h} + \delta e^{\sigma}$; this effectively reduces to a

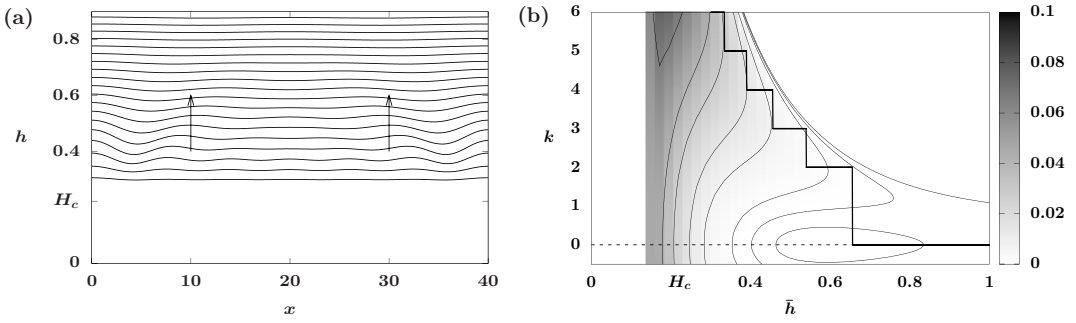

FIG. 7. (a) Condensation dynamics with transient pattern formation starting from the initial data $h_0(x) = 0.3 + 0.001\sum_{k=1}^{6}\cos(2k\pi x/L)$ with $L = 40$ and other parameters identical to Fig. 5. (b) Contour plot of the growth rate $d\sigma/dt$ with the thick line representing the computed most unstable wave number k^* as the condensation occurs.

sensitivity analysis for (8a) with respect to the evolving base state $\bar{h}(t)$: $d\sigma/dt = -\beta\tilde{J}'(\bar{h})$. Similar analysis for the stability of dewetting evaporating thin films was also done in [18]. The transition between these $\bar{h}$-dependent forms of dispersion relations occurs at $k^* = 0$ and appears similar to the type-II and type-III instabilities described in [50]. The significant qualitative changes in the dispersion relation as $\bar{h}(t)$ evolves show that the frozen-time approximation cannot be expected to give good predictions for the dynamics in the critical pressure regime.

In Fig. 7 we demonstrate that under the same system parameters, starting with a thicker film ($\langle h_0\rangle = 0.3 > H_c$) yields condensation. With $P_0 = 0.5$ in the critical range, the numerical simulation for (1) starting from the weakly perturbed film (initial profile given in the figure caption) shows monotonic growth of the mass. The apparent most unstable wave number k^* is numerically tracked by using the Fourier transform of the time derivative of the PDE solution $\partial h/\partial t$ and is plotted against the average film thickness. Starting from $k^* = 6$, the evolution going down to $k^* = 0$ is shown overlaid on the contour lines of the dispersion relation (8b) and follows the linear prediction well. This is expected, since while there may be some transient growth of spatial modes, as condensation continues and $\bar{h}(t)$ increases further, the perturbations are relatively small in amplitude and will also eventually decay out. So transient pattern formation also can occur in condensation, but it is not as dramatic as in evaporation.

The long-time behavior for condensation is unbounded growth of the film thickness (sometimes called flooding), where $\bar{h} \to \infty$. In this limit, Eq. (8a) requires $P_0 > 0$ and hence this behavior only occurs in the critical and supersaturated cases, with the flux reducing to $\tilde{J} \sim -P_0/\bar{h}$. For $\bar{h} \to \infty$, (8b) reduces to $d\sigma/dt \sim -\bar{h}^3(2k\pi/L)^4$, namely, for all β (and all $P_0 > 0$), spatial perturbations will decay due to surface tension and flooding will always be manifested in terms of flat films following the leading-order behavior

$$\frac{d\bar{h}}{dt} \sim \frac{\beta P_0}{\bar{h}} \Rightarrow \bar{h}(t) \sim \sqrt{2\beta P_0 t} \quad \text{for } t \to \infty. \tag{18}$$

IV. NONUNIFORM STEADY STATES

Recalling the energy (4), all steady states of (1) have zero pressure and the periodic nonuniform steady states satisfy the boundary-value problem on $0 \leqslant x \leqslant L$,

$$\frac{d^2h}{dx^2} - \Pi(h) = 0, \quad h(0) = h(L), \quad h'(0) = h'(L). \tag{19}$$

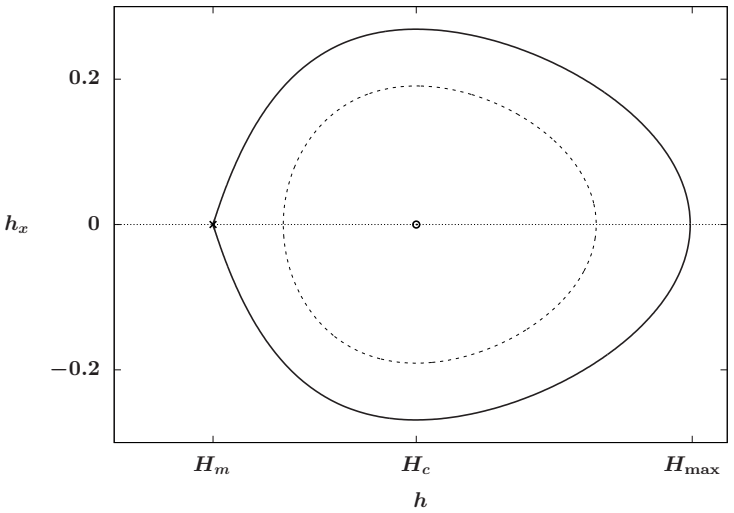

FIG. 8. Phase plane for the second-order steady-state solutions satisfying (19) in the critical case with $0 < P_0 < \mathcal{P}_\epsilon$. The homoclinic orbit (solid line) corresponds to the droplet solution in Fig. 9(a) and the dashed line represents the periodic solution in Fig. 9(b).

For the undersaturated case with $P_0 < 0$ and the supersaturated case with $P_0 > \mathcal{P}_\epsilon$, Eq. (19) does not have any nonuniform solutions. In this section we will obtain nontrivial periodic solutions to (19) that exist only for the critical case with $0 < P_0 < \mathcal{P}_\epsilon$.

Steady states of the mass-conserving thin-film equation satisfy the same form of second-order differential equation problem (19). For the conservative problem with $\beta = 0$, P_0 in (1e) is a free parameter that parametrizes the continuous family of coexisting steady states. For the nonconservative model (1) with $\beta > 0$, P_0 is an imposed system parameter that determines a unique nonuniform steady state on a given domain.

With different forms of $\tilde{\Pi}(h)$ in (1e), the steady states and stability of conservative thin-film equations have been the focus of many studies. In [41] Bertozzi *et al.* considered the steady states using the regularized disjoining pressure $\tilde{\Pi}(h) = Ah^{-3}(1 - \epsilon/h)$. Laugesen and Pugh studied the properties and energy levels of positive steady states for a generalized conservative thin-film equation with $\tilde{\Pi}(h) = h^{-\alpha}$ [51,52] and provided linear stability results for a nonconservative thin-film model with a linear fourth-order term [53]. In [52] Laugesen and Pugh showed that the linear stability of even steady states that satisfy periodic boundary conditions on $(0,L)$ is equivalent to the linear stability of the steady states with respect to the Neumann (or no-flux) boundary conditions over the half domain $0 \leqslant x \leqslant L/2$.

The phase plane of (h,h_x) is plotted in Fig. 8, where the equilibrium $H_m(P_0)$ is a saddle point and $H_c(P_0)$ is a center point. Picking a value of the minimum height $h_{\min}$ in the range $H_m \leqslant h_{\min} \leqslant H_c$ determines a contour in the phase plane describing a periodic steady-state solution. For each value of $h_{\min}$, the corresponding maximum height $h_{\max}$ comes from $U(h_{\max}) = U(h_{\min})$. In particular, if $h_{\min} = H_m$, we have a homoclinic orbit through the saddle point H_m which corresponds to a solitary droplet solution shown in Fig. 9(a). The maximum height $H_{\max}$ of the droplet is then given by the root of $U(H_{\max}) = U(h_{\min})$, which for $\epsilon \to 0$ can be written as

$$H_{\max} = \frac{1}{6P_0} + \epsilon + O(\epsilon^2). \tag{20}$$

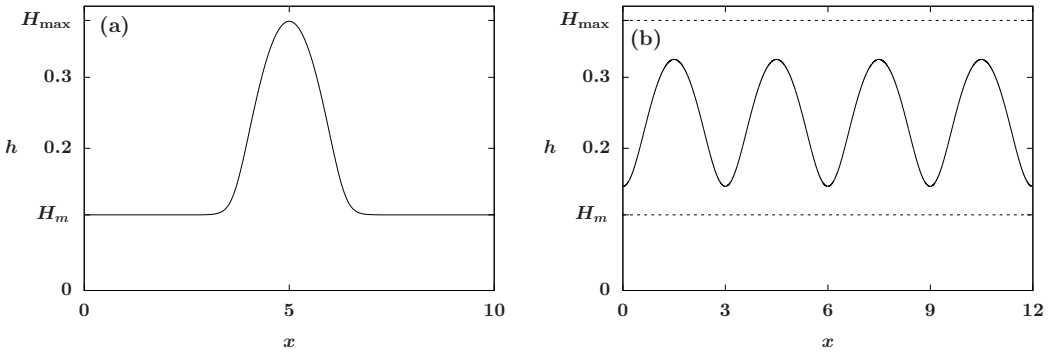

FIG. 9. (a) Typical steady-state droplet solution and (b) a periodic solution satisfying the ODE (19).

For $H_m < h_{\min} < H_c$, we have periodic steady-state solutions with a typical plot presented in Fig. 9(b). The length of the period $\ell(h_{\min})$ of the periodic steady state $h(x)$ can be obtained by

$$\ell(h_{\min}) = \int_0^{\ell(h_{\min})} dx = 2\int_{h_{\min}}^{h_{\max}} \frac{1}{\sqrt{2U(s) - 2U(h_{\min})}} ds. \tag{21}$$

Small-amplitude periodic steady-state solutions h bifurcate from the spatially uniform steady state H_c [18]. Using linear stability at H_c, it can be shown [41,54] that the minimum period of oscillations is given by

$$\ell_s = \frac{2\pi}{\sqrt{-\Pi'(H_c)}}. \tag{22}$$

Equation (21) defines a monotonic function on $h_{\min}$ satisfying

$$\ell(h_{\min} \to H_c) = \ell_s, \quad \ell(h_{\min} \to H_m) \to \infty.$$

We define primary periodic steady-state solutions with a single maximum on the domain $0 \leqslant x \leqslant L$ as $h = H_s(x)$. Figure 10 shows that the average thickness $\langle H_s \rangle$, parametrized by L, bifurcates from H_c at $L = \ell_s$. Since $H_s(x)$ approaches a finite-mass solitary droplet, we have $\lim_{L\to\infty}\langle H_s\rangle = H_m$.

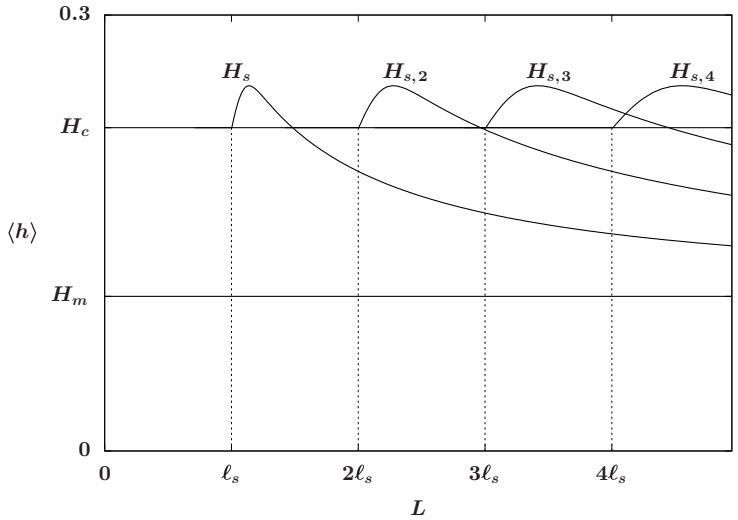

FIG. 10. Bifurcation diagram for $\langle h \rangle$ parametrized by the domain size L with the parameter $P_0 = 0.5$.

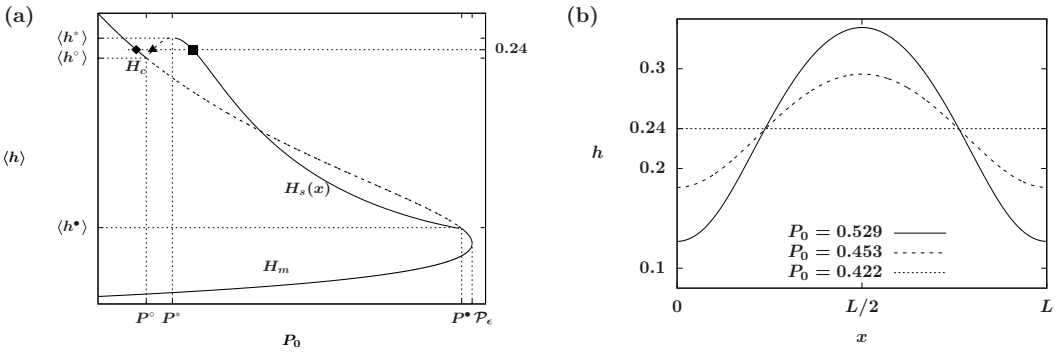

FIG. 11. (a) Bifurcation diagram of steady states to (19) with the domain size $L = 3.05$ showing that a family of nonuniform steady states coexists with the constant steady states H_m and H_c in a specific range of P_0. The solid lines represent the stable steady states and the dashed lines correspond to the unstable ones. (b) Coexisting equilibria of (19) with the average film thickness $\langle h \rangle = 0.24$ and the domain size $L = 3.05$.

Higher-order families of nonuniform steady states $H_{s,k}(x)$ with k periods bifurcating from H_c at $L = k\ell_s$ for $k = 2,3,\ldots$ are also shown in Fig. 10. Multiple periodic nonuniform steady states can coexist on a given domain with $L \geqslant 2\ell_s$.

The value of the system parameter P_0 is also important in selecting between multiple coexisting periodic steady states $H_s(x)$. With a fixed domain size $L = \ell = 3.05$, a bifurcation diagram of the average film thickness of steady states satisfying (19) with respect to P_0 is presented in Fig. 11(a). It shows that in addition to the constant steady states $h \equiv H_c$ and $h \equiv H_m$, a family of nonuniform steady-state solutions $H_s(x)$ exists for $P^\circ \leqslant P_0 \leqslant P^\bullet$ bifurcating from the uniform steady state H_c at $P_0 = P^\circ$ and $P_0 = P^\bullet$. These two bifurcation points can be obtained by setting $\ell_s = L$ and solving (22) for the P_0 values. Moreover, there exists a critical $P^* = P^*(\ell)$ such that for $P^* < P_0 < P^\bullet$ the average thickness $\langle H_s \rangle$ of $H_s(x)$ is monotonically decreasing with respect to the parameter value P_0, while for $P^\circ < P_0 < P^*$ we have $\langle H_s \rangle$ increasing with P_0. The maximum value $\langle H^* \rangle$ of the average thickness is attained at $P_0 = P^*$ and the average thickness of small-amplitude steady-state solutions are given by $\langle H^\circ \rangle$ and $\langle H^\bullet \rangle$ at $P_0 = P^\circ$ and $P_0 = P^\bullet$, respectively.

The above bifurcation diagram also characterizes the coexistence of steady states with given length of period and average film thickness. Specifically, it indicates that for $\langle H^\circ \rangle < \langle h \rangle < \langle H^* \rangle$, two nonuniform steady states and the uniform state H_c coexist. An example of coexisting steady states with $\langle h \rangle = 0.24$ is shown in Fig. 11(b), which corresponds to three marked dots in Fig. 11(a). This is consistent with the results obtained in [51] on the existence and uniqueness of steady-state solutions of the mass-conserving thin-film model with specific domain size and average thickness.

V. STABILITY ANALYSIS OF NONUNIFORM STEADY STATES

In the preceding section we have studied the steady states and in this section we focus on their linear stability and transient behavior. We consider a positive ℓ-periodic steady state $H_s(x)$ over the domain $0 \leqslant x \leqslant L$ and perturb it by setting $h(x,t) = H_s(x) + \delta\Psi(x)e^{\lambda t}$, where $\delta \ll 1$ and $\Psi(x)$ is also ℓ periodic. Since $H_s(x)$ satisfies the ODE (19), we linearize Eq. (1) around the steady state $H_s(x)$ and obtain the $O(\delta)$ equation

$$\lambda\Psi = \mathscr{L}\Psi, \tag{23}$$

where the linear operator $\mathscr{L}$ is

$$\mathscr{L}\Psi \equiv \left[-\frac{\beta}{H_s + K_0} + \frac{d}{dx}\left(H_s^3\frac{d}{dx}\right)\right]\left(\Pi'(H_s)\Psi - \frac{d^2\Psi}{dx^2}\right). \tag{24}$$

We rewrite this fourth-order operator as the product of two second-order operators

$$\mathscr{L}\Psi = \mathcal{Q}\mathcal{P}\Psi, \tag{25}$$

where $\mathcal{Q}$ is an operator that includes the evaporative flux and the mobility

$$\mathcal{Q}w \equiv -\frac{\beta w}{H_s + K_0} + \frac{d}{dx}\left(H_s^3 \frac{dw}{dx}\right) \tag{26}$$

and $\mathcal{P}$ is the linearized pressure operator

$$\mathcal{P}v \equiv \Pi'(H_s)v - \frac{d^2 v}{dx^2}. \tag{27}$$

The operator $\mathscr{L}$ is not self-adjoint with respect to the standard L^2 inner product; the adjoint operator $\mathscr{L}^\dagger$ is given by

$$\mathscr{L}^\dagger \Phi \equiv \mathcal{P}\mathcal{Q}\Phi. \tag{28}$$

If there are any positive eigenvalues λ to the problem (23), then the steady state $H_s(x)$ is unstable. In Sec. V A we will study this eigenvalue problem for the conservative model with $\beta = 0$ where $\mathscr{L}$ in (24) reduces to a simpler operator. Then, through an operator expansion in the limit $\beta \to 0$, we obtain the stability of the nonuniform steady states in Sec. V B. For simplicity in this section we only focus on the case where a one-period solution fits in the domain, that is, $L = \ell$, but this framework can be easily extended to solutions with multiple periods.

A. Linear stability of the conservative PDE with $\beta = 0$

The linear stability analysis of the steady states of the conservative PDE with $\beta = 0$ is important to the understanding of the stability of equilibria of the model (1) with $\beta \ll 1$, so here we begin with a brief overview of the stability of the steady states of the model [41]. We will derive a critical domain size $L = \ell^*$ where the stability of the steady states changes for $\beta = 0$.

The linear stability of these nonuniform steady states $H_s(x)$ can be obtained by solving the eigenproblem (23), which by using $\beta = 0$ reduces to

$$\mathscr{L}_0\Psi = \lambda\Psi, \quad \text{where } \mathscr{L}_0\Psi \equiv \frac{d}{dx}\left[H_s^3 \frac{d}{dx}(\mathcal{P}\Psi)\right]. \tag{29}$$

We numerically solve this eigenproblem for the steady states presented in Fig. 11(a) and show that for the range $P^* < P_0 < P^\bullet$ the family of nonuniform steady states is stable. It coexists with the branch of spatially uniform unstable steady state $h \equiv H_c$ and becomes unstable for $P^\circ < P_0 < P^*$. While the stability of the uniform steady states $h \equiv H_m$ is independent of P_0, the other steady state $h \equiv H_c$ is only stable in the ranges $P^\bullet < P_0 < \mathcal{P}_\epsilon$ and $P_0 < P^\circ$ and is unstable for $P^\circ < P_0 < P^\bullet$, where the nonuniform steady state exists. This difference from the stability of H_c described in Sec. III is due to the conservation-of-mass condition for $\beta = 0$ (eliminating the $k = 0$ mode) and periodic boundary conditions on a finite domain selecting discrete modes.

Numerical evidence suggests that the critical value P^* is monotonically decreasing with respect to ℓ for $\ell > \ell_s$. Therefore, given a fixed value of the parameter P_0, there exists a critical period ℓ^* such that $P^*(\ell^*) = P_0$. Then, for any period ℓ in the range of $\ell_s < \ell < \ell^*$, we have $P^*(\ell) > P^*(\ell^*) = P_0$. This indicates that the corresponding steady state $H_s(x)$ with the period ℓ and average film thickness $\langle H_s \rangle$ is unstable with a positive eigenvalue λ to the eigenproblem (29). There coexists another steady state which is stable with $P_0 > P^*(\ell)$ with the same period ℓ and average film thickness $\langle H_s \rangle$. On the other hand, for $\ell > \ell^*$ with $P^*(\ell) < P^*(\ell^*) = P_0$, there exists a stable steady state $H_s(x)$ and the corresponding steady state with $P_0 < P^*(\ell)$ is unstable.

For the parameter $P_0 = 0.5$, we numerically calculate the corresponding critical period as $\ell^* = 3.005$. With this parameter choice in Fig. 12 we plot the two largest eigenvalues of the eigenproblem (29) for the nonuniform steady state $H_s(x)$ over a range of periods ℓ. In addition to the $\lambda = 0$

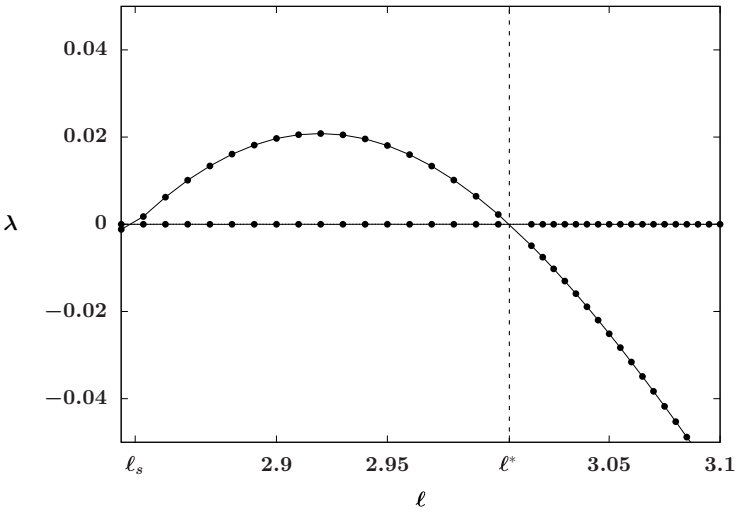

FIG. 12. Dependence of dominant eigenvalues of $H_s(x)$ on the period ℓ for the eigenproblem (29) with $P_0 = 0.5$, where the critical period is given by $\ell^* = 3.005$.

translational mode, for $\ell_s < \ell < \ell^*$ we have a positive eigenvalue making H_s unstable, while for $\ell > \ell^*$ H_s is stable.

The relationship between the period of a given steady state and the critical length of period ℓ^* is important to the stability of the PDE (1) for both the cases $\beta = 0$ and $\beta \neq 0$. In the following section we focus on the influence of weak nonconservative effects and for $\beta > 0$ we will see the same change in stability at $\ell = \ell^*$.

B. Nonuniform steady states: Linear stability with $\beta \to 0$

For nonuniform steady states $H_s(x)$ with $\beta \neq 0$ we first derive some properties for the eigenfunctions of $\mathscr{L}$ [Eq. (23)] and then characterize its dominant eigenmodes using an asymptotic operator expansion as $\beta \to 0$. By taking the L^2 inner product of $\mathscr{L}\Psi$ and $\mathcal{P}\Psi$, integration by parts, and using $\beta > 0$ then leads to

$$\langle \mathscr{L}\Psi, \mathcal{P}\Psi \rangle = -\beta \int_0^L \frac{(\mathcal{P}\Psi)^2}{H_s + K_0} dx - \int_0^L H_s^3 \left[\frac{d}{dx}(\mathcal{P}\Psi) \right]^2 dx \leqslant 0. \tag{30}$$

Applying (23) to the inner product and using integration by parts, one gets

$$\langle \mathscr{L}\Psi, \mathcal{P}\Psi \rangle = \lambda \langle \Psi, \mathcal{P}\Psi \rangle = \lambda \int_0^L \Pi'(H_s)\Psi^2 + \Psi_x^2 dx. \tag{31}$$

Combining (30) and (31), we conclude that the eigenfunctions associated with positive eigenvalues $\lambda > 0$ satisfy

$$\int_0^L \Pi'(H_s)\Psi^2 + \Psi_x^2 dx \leqslant 0.$$

Moreover, if $\lambda = 0$, then the two integrals in (30) indicate that the eigenfunction Ψ associated with zero eigenvalue is determined by

$$\mathcal{P}\Psi \equiv \Pi'(H_s)\Psi - \frac{d^2\Psi}{dx^2} = 0. \tag{32}$$

The solution of (32) leads to a translational eigenfunction associated with zero eigenvalue, $\Psi^T = \frac{dH_s}{dx}$.

For the special case with $\beta = 0$ when P_0 can take a continuous range of values, there is an additional eigenfunction $\Psi_0^P = \frac{dH_s}{dP_0}|_{\beta=0}$ in the null space of the linearized operator $\mathscr{L}$. Taking the derivative of (19) with respect to P_0 yields $\mathcal{P}\Psi_0^P = 1$, which then leads to $\mathscr{L}\Psi_0^P = \mathcal{Q}(1) = 0$.

To understand the dependence of the spectrum of $\mathscr{L}$ on the parameter β, we consider the asymptotic expansions as $\beta \to 0$,

$$\Psi = \Psi_0 + \beta\Psi_1 + \cdots, \quad \lambda = \lambda_0 + \beta\lambda_1 + \cdots. \tag{33}$$

Substituting these expansions into the eigenproblem (23) leads to the $O(1)$ problem

$$\mathscr{L}_0\Psi_0 = \lambda_0\Psi_0, \tag{34}$$

which is equivalent to the eigenproblem (29) for the conservative thin-film equation (41) without any mass-conservation constraint. It has been shown in [11,55] that the linear operator $\mathscr{L}_0$ is self-adjoint with respect to a weighted H^{-1}-norm. Therefore, from spectral theory, for a compact domain the associated spectrum of the leading-order eigenvalue problem (34) is real and discrete. The $O(\beta)$ problem can be written as

$$\mathscr{L}_0\Psi_1 - \lambda_0\Psi_1 = \frac{\mathcal{P}\Psi_0}{H_s + K_0} + \lambda_1\Psi_0. \tag{35}$$

Integrating (34) over the domain gives

$$\lambda_0 \int_0^L \Psi_0 dx = 0, \tag{36}$$

from which we see that any nonzero eigenvalue of (34) leads to a zero-mean eigenfunction, and if Ψ_0 has a nonzero mean then the corresponding $\lambda_0 = 0$. The translational mode $\Psi_0^T = \frac{dH_s}{dx}$ has a zero mean due to the periodic boundary conditions and $\lambda_0^T = 0$. The pressure mode $\Psi_0^P = \frac{dH_s}{dP_0}|_{\beta=0}$ has $\lambda_0^P = 0$ and a nonzero mean. We denote the largest nonzero eigenvalue by λ_0^V, whose associated eigenmode Ψ_0^V has zero mean and leads to growth or decay of spatial variations from the mean of the solution $h(x,t)$.

For the translational eigenfunction Ψ^T the expansion (33) is trivial since this branch of zero eigenvalue is independent of the value of β and exists for any periodic solutions. For the second eigenfunction Ψ^P we can integrate (35) over the domain and apply the periodic boundary conditions to obtain

$$\lambda_1^P = -\frac{1}{\langle \Psi_0^P, 1\rangle}\left\langle \frac{\mathcal{P}\Psi_0^P}{H_s + K_0}, 1\right\rangle.$$

For the Ψ^V mode, integrating (35) over $0 \leqslant x \leqslant L$ and applying (36) then yields

$$\int_0^L \Psi_1^V dx = -\frac{1}{\lambda_0^V}\int_0^L \frac{\mathcal{P}\Psi_0^V}{H_s + K_0} dx. \tag{37}$$

This is not guaranteed to be zero, therefore, for $\beta \neq 0$ we expect to have eigenfunctions of (23) with nonzero means which account for the loss or gain of mass in the dynamics. Moreover, in this case λ_1^V can be determined by applying the solvability condition to (35). Note that the adjoint operator $\mathscr{L}_0^\dagger$ of the leading-order operator $\mathscr{L}_0$ takes the form $\mathscr{L}_0^\dagger\Phi_0^V \equiv (\mathcal{P}\mathcal{Q}|_{\beta=0})\Phi_0^V$, where the eigenfunction of the adjoint operator associated with the leading-order eigenvalue λ_0^V is denoted by Φ_0^V. Taking the inner product of Φ_0^V with the right-hand side of (35) gives

$$\lambda_1^V = -\frac{1}{\langle \Psi_0^V, \Phi_0^V\rangle}\left\langle \frac{\mathcal{P}\Psi_0^V}{H_s + K_0}, \Phi_0^V\right\rangle. \tag{38}$$

We now investigate the linear stability of the nonuniform steady state $H_s(x)$ where the domain size L is in the range of either $L > \ell^*$ or $\ell_s < L < \ell^*$. Specifically, we are interested in the bifurcation

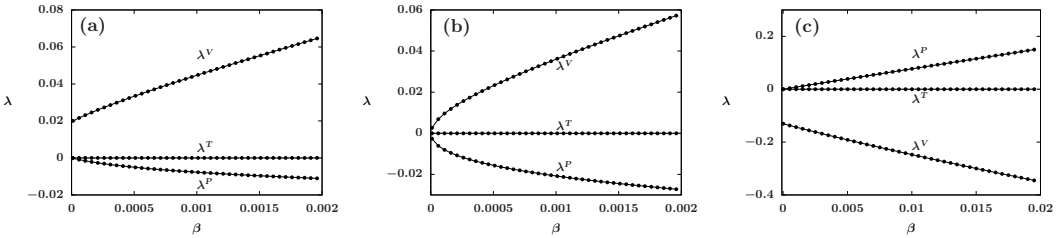

FIG. 13. Plots of the largest three eigenvalues of (23) over a range of β with the period ℓ satisfying (a) $\ell = 2.9 < \ell^*$, (b) $\ell = 3.005 = \ell^*$, and (c) $\ell = 3.2 > \ell^*$. The critical period is $\ell^* \approx 3.005$ for $P_0 = 0.5$.

of the eigenproblem (23) parametrized by β in the limit of $\beta \to 0$. Recall from Sec. V A that the parameter $P_0 = 0.5$ corresponds to the critical $\ell^* = 3.005$. We will use this parameter value for the following discussion. To demonstrate that $\ell^* = 3.005$ is indeed a critical value for the nonuniform steady state $H_s(x)$, we numerically calculate the dominant eigenvalues of the eigenproblem (23) with $\ell^* = 3.005$ and $0 \leqslant \beta \leqslant 0.002$. The eigenvalues are plotted in Fig. 13(b), showing that the three branches of eigenvalues come together at $\beta = 0$.

For $\ell > \ell^*$, the dominant eigenvalues of the ℓ-periodic steady state $H_s(x)$ are plotted against β in Fig. 13(c). It shows that in the limit $\beta \to 0$, the nonuniform steady state $H_s(x)$ is unstable to the Ψ^P mode with $\lambda^P \sim \lambda_1^P \beta$ as $\beta \to 0$ where $\lambda_1^P > 0$, while for $\ell_s < \ell < \ell^*$, the plot in Fig. 13(a) indicates that the unstable eigenvalue λ^V takes the form $\lambda^V \sim \lambda_0^V + \lambda_1^V \beta$ as $\beta \to 0$ where $\lambda_0^V, \lambda_1^V > 0$.

For solutions with multiple droplets, additional unstable zero-mean coarsening modes that account for symmetry breaking and droplet merging coexist with the dominant modes described above [56]. We will consider the simplest case for steady states with two droplets where there is only one symmetry-breaking mode Ψ^B and one droplet-merging mode Ψ^M.

VI. NUMERICAL SIMULATIONS

To understand the significance of the stability of the nonuniform equilibria, we focus on the effects of the unstable eigenmodes of $H_s(x)$ based on PDE simulations of (1) starting from initial conditions of the form

$$h_0(x) = H_s(x) + \delta\Psi(x), \tag{39}$$

where $\Psi(x)$ is a normalized eigenmode associated with a positive eigenvalue λ and $\|\Psi\|_2 = 1, \Psi(0) \geqslant 0$, and $|\delta| \ll 1$. Since it is assumed that the solution takes the form of $h(x,t) \sim H_s(x) + \delta\Psi(x)e^{\lambda t}$ when it is close to the steady state, the growth or decay of the perturbation in time can be quantified by

$$\|h(x,t) - H_s(x)\|_2 = \delta\|\Psi\|_2 e^{\lambda t} + O(\delta^2).$$

Unless stated otherwise, for all the simulations in this section, we set $\beta = 0.001$ and $P_0 = 0.5$.

We begin by studying the dynamics from a single-drop steady state $H_s(x)$. We use a numerical example to illustrate how the nonconservative eigenfunctions are tied to the evaporation dynamics. With $\ell = L = 3.0$ satisfying $\ell_s < \ell < \ell^*$, the eigenproblem for the nonuniform steady state H_s has only one positive eigenvalue $\lambda^V = 0.03744$. Starting from the initial data $\lambda^V = H_s - 0.0001\Psi^V$, evaporation occurs and the solution eventually converges to the stable spatially uniform steady state $h = H_m$ (see Fig. 14). Although the initial condition has average height $\langle h_0 \rangle > H_c$, suggestive of filmwise condensation based on (8a), the strong influence of the spatial profile leads to dropwise evaporation. In the early stage, Fig. 14(a) shows that the spatial variations increase as the peak of the solution increases while minima decrease, and the growth rate of $\|h - H_s\|_2$ is consistent with the predicted growth rate given by the unstable eigenvalue λ^V (see Fig. 15). In the later stage the convergence rate to the uniform steady state $h = H_m$ agrees with the analytical prediction from (12)

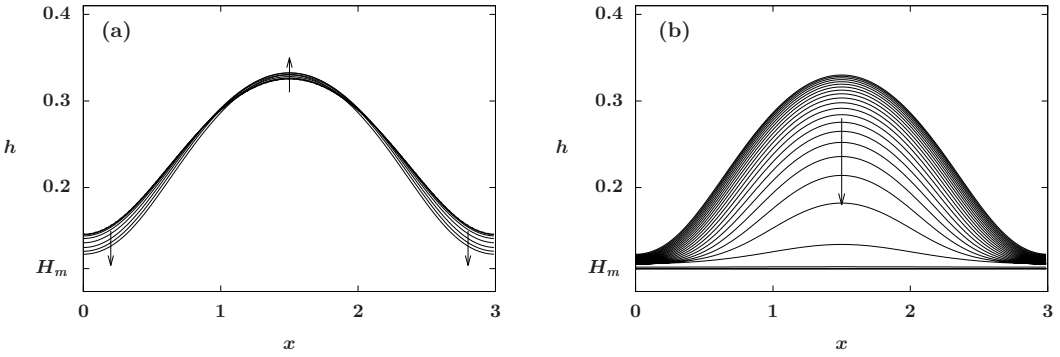

FIG. 14. (a) Early-stage evolution ($0 \leqslant t < 250$) and (b) the later stage ($t > 250$) of evaporation with the initial condition close to the nonuniform steady-state solution H_s for a PDE simulation starting from the initial data $h_0(x) = H_s - 0.0001\Psi^V$ with domain size $L = \ell = 3$.

with the wave number $k = 0$, $\lambda^m = -\beta\Pi'(H_m)/(H_m + K_0) = -0.286\,79$. If the simulation starts with $\lambda^V = H_s + 0.0001\Psi^V$ instead, then condensation with decreasing spatial variations occurs, eventually leading to flooding (18).

Now we study the more complicated dynamics that can occur with multiple droplets. For simplicity, only two-droplet steady states will be investigated. We consider the nonuniform steady state $H_{s,2}(x)$ with the period $\ell = 3.5 > \ell^*$ on $0 \leqslant x \leqslant 7$. By numerically solving the eigenproblem (23), we obtain three unstable eigenmodes (see Fig. 16) in addition to the translational zero eigenmode (not shown).

The eigenvalue $\lambda^B = 0.007\,36$ corresponds to the coarsening mode Ψ^B that leads to symmetry breaking, $\lambda^M = 0.006\,11$ corresponds to the eigenmode Ψ^M that yields droplet merging, and $\lambda^P = 0.005\,28$ is associated with the mode Ψ^P that corresponds to evaporation or condensing effects. Among the three unstable eigenmodes, the only mode with nonzero mean is the Ψ^P that yields evaporative effects; the other two eigenmodes govern the dynamics that conserve mass.

The set of PDE simulations in Fig. 17 demonstrates the effects of these eigenmodes as the initial conditions (39) with perturbation amplitude $\delta = 0.1$. With $\Psi(x) = \Psi^B$, initial perturbations lead to mass increase of the left droplet while the droplet on the right shrinks in time, breaking the symmetry of the original state [see Fig. 17(a)]. For $\Psi(x) = \Psi^M$ as the perturbation, the two droplets with the period $\ell = 3.5$ merge into one larger droplet with the period $\ell = 7$ [see Fig. 17(b)]. These two

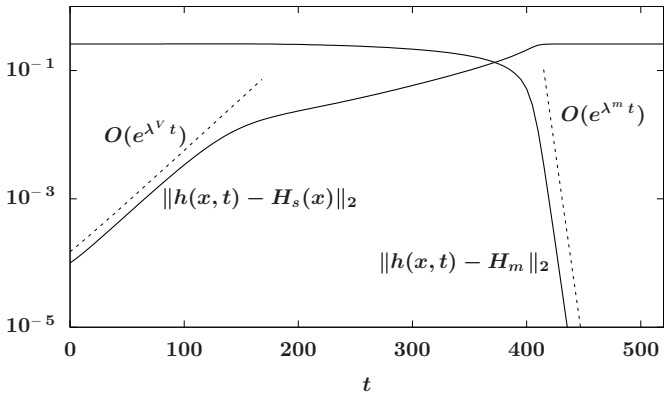

FIG. 15. Growth and decay rates of the L^2-norms between the PDE solution shown in Fig. 14 and the steady states $H_s(x)$ and H_m, showing that the solution evolves from the $H_s(x)$ state towards H_m.

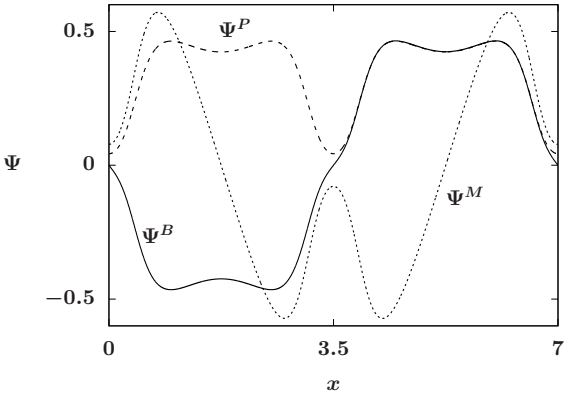

FIG. 16. Unstable eigenmodes of the nonuniform steady state $H_{s,2}(x)$ with two zero-mean modes Ψ^B and Ψ^M and a nonzero-mean mode Ψ^P where the domain size $L = 2\ell = 7$ and the other system parameters are identical to those in Fig. 14.

examples are similar to the coarsening dynamics observed in conservative thin-film models [56]. In Fig. 17(c) we show the results for the perturbation $\Psi = \Psi^P$ where initially spatial variations decrease. The solution eventually evolves into a spatially uniform film which grows indefinitely in

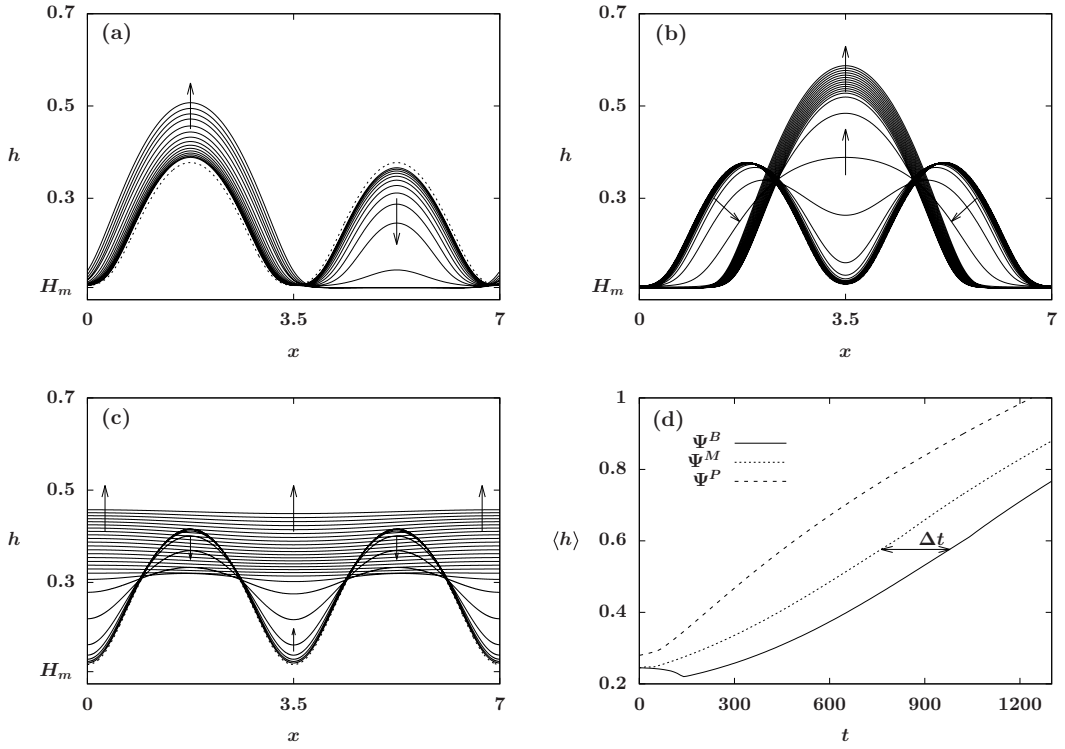

FIG. 17. The PDE simulations of two droplets on $0 \leqslant x \leqslant 7$ starting from $h_0(x) = H_{s,2}(x) + 0.1\Psi$ showing (a) symmetry breaking with $\Psi = \Psi^B$, (b) droplet merging with $\Psi = \Psi^M$, and (c) flattening with $\Psi = \Psi^P$. (d) Corresponding changes of $\langle h \rangle$ in time, where the long-time behavior of the solutions perturbed by the Ψ^B mode is identical to that of the Ψ^M mode shifted by $\Delta t = 217$.

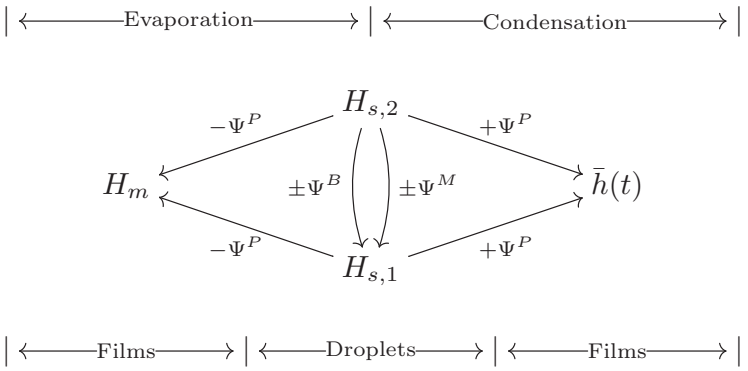

FIG. 18. Transition-state diagram connecting linearized dynamics in the small-domain case with $\ell < \ell^*$.

time. This flooding dynamics will also occur at later times for the simulations from Figs. 17(a) and 17(b) with $\bar{h}(t) = O(t^{1/2})$ following (18), similar to Fig. 19.

The evolving average film thickness $\langle h \rangle$ of the three simulations is plotted in Fig. 17(d), showing that among the three eigenmodes Ψ^P yields the fastest condensation, while the dynamics driven by the two zero-mean modes are delayed by the early-stage coarsening. Solutions from all these simulations are approaching flat films governed by the large thickness limit (8a). Both Figs. 17(a) and 17(b) proceed by coarsening to a growing single drop and then leading to flooding. They differ in the position and formation time of that drop, but the flooding behavior is the same except for a time shift of $\Delta t = 217$ between the two.

Figure 18 gives a transition diagram that summarizes the relations between the instabilities and dynamics of the coexisting states studied above in a small domain for $\ell > \ell^*$. Droplet steady states $H_{s,1}$ and $H_{s,2}$ perturbed by the eigenmode Ψ^P either converge to the constant equilibrium H_m (see Fig. 14) or exhibit filmwise condensation [see Fig. 17(c)]. The two coarsening modes Ψ^B and Ψ^M account for the transition from $H_{s,2}$ to $H_{s,1}$ up to a spatial translation [see Figs. 17(a) and 17(b)]. For droplets states with periods in the range of $\ell_s < \ell < \ell^*$, the stability of some of the eigenmodes can change and the transition from droplets to flat films can be induced by the Ψ^V mode. While filmwise dynamics with an increasing or decreasing total mass are relatively straightforward to understand (see Sec. III), whether droplet states and coarsening dynamics will lead to evaporation or condensation is more difficult to identify.

With a larger domain size, more complicated dynamics are expected and need further investigation. With more droplet states involved, more unstable coarsening and flattening modes will appear in the corresponding transition diagram. Figure 19 shows the dynamics of (1) starting from a typical initial profile $h_0(x) = 0.2 - 0.03\sin(6\pi x/L) + 0.01\sin(4\pi x/L)$ on the periodic domain $0 \leqslant x \leqslant L$ with $L = 20$. Initially, the long-wave instability due to the disjoining pressure $\Pi(h)$ yields coalescence of the film into three isolated droplets connected by a thin layer $h \sim \epsilon$. Due to the competition between the evaporation effects and the disjoining pressure, the right and the left droplets collapse sequentially to the thin layer, followed by the slow condensation of the center droplet. This dropwise condensation mode then transitions to filmwise condensation as the condensing droplet reaches the size of the domain. Moreover, it is shown in Fig. 20 that making a small perturbation (changing $\langle h_0 \rangle$) to the initial conditions used in (19) can lead to very different droplet dynamics than presented in Fig. 19. Instead of dropwise and filmwise condensation, the three isolated droplets all collapse for long times, indicating that the dynamics are sensitive to the initial conditions.

Motivated by the different dynamics shown in Figs. 19 and 20, we now more systematically explore the dependence of evaporation versus condensation on initial conditions and the β value. The plot in Fig. 21 shows simulation results starting from the family of initial conditions

$$h_0(x) = \bar{h}_0 - 0.03\sin(6\pi x/L) + 0.01\sin(4\pi x/L), \tag{40}$$

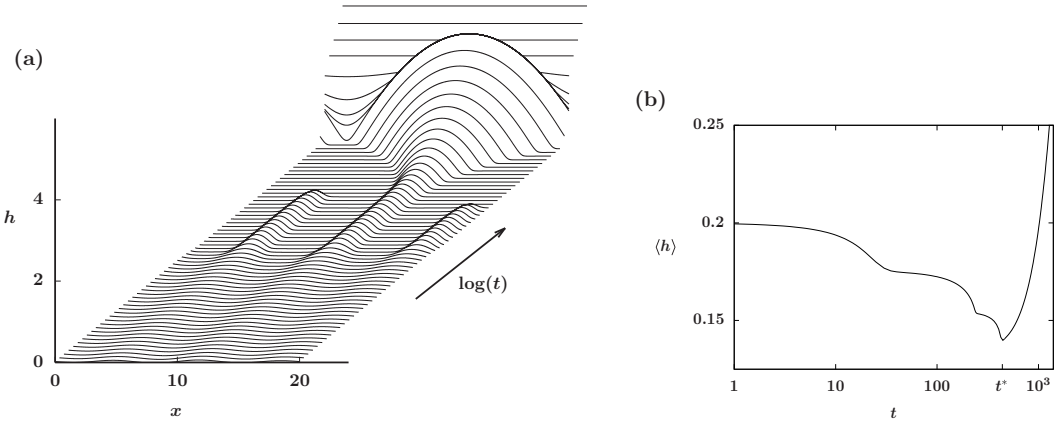

FIG. 19. (a) Numerical simulation of dewetting of a volatile thin film starting from typical initial conditions: early-stage dewetting yielding three metastable droplets, subsequent collapse of the left and right droplets occurring while the center droplet gradually grows, followed by filmwise condensation after the substrate is flooded. (b) Plot showing the average thickness $\langle h \rangle$ decreasing in the early regime for $0 \leqslant t < t^* \approx 440$ corresponding to dewetting and evaporation, with later condensation yielding increasing average thickness for $t > t^*$.

parametrized by a range of values for $\bar{h}_0$ on the domain $0 \leqslant x \leqslant L$ with $L = 20$. We also use a range of values for β in (1) to examine the impact of weak versus strong evaporation relative to dewetting effects. For each simulation with a given $(\beta,\bar{h})$, the observation of long-time evaporation or condensation is labeled by open or closed circles, respectively, in Fig. 21. For large $\bar{h}$ the dynamics rapidly converges to filmwise condensation, while sufficiently small $\bar{h}$ leads to evaporation. For a given β, there is an intermediate range of $\bar{h}$ at which we observe early-stage coarsening dynamics followed by dropwise evaporation or condensation dynamics, similar to the evolutions shown in Figs. 19 and 20. We use a simple curve to indicate the separate regions of observed evaporation and condensation dynamics. These simulation results for finite-amplitude initial conditions are not obvious from the linear stability results for infinitesimal perturbations (Sec. III), which would suggest that the dividing curve be the constant $\bar{h}_0 = H_c$ for all β. We suspect that the separation curve approaches H_c as $\beta \to \infty$.

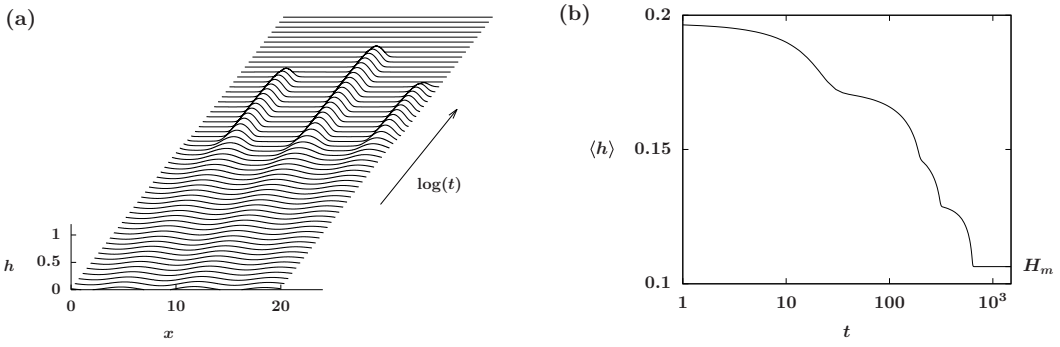

FIG. 20. (a) The PDE simulation starting from initial data $h_0(x) = 0.197 - 0.03\sin(6\pi x/L) + 0.01\sin(4\pi x/L)$ for the model (1) and (b) the corresponding monotonically decreasing average thickness in time.

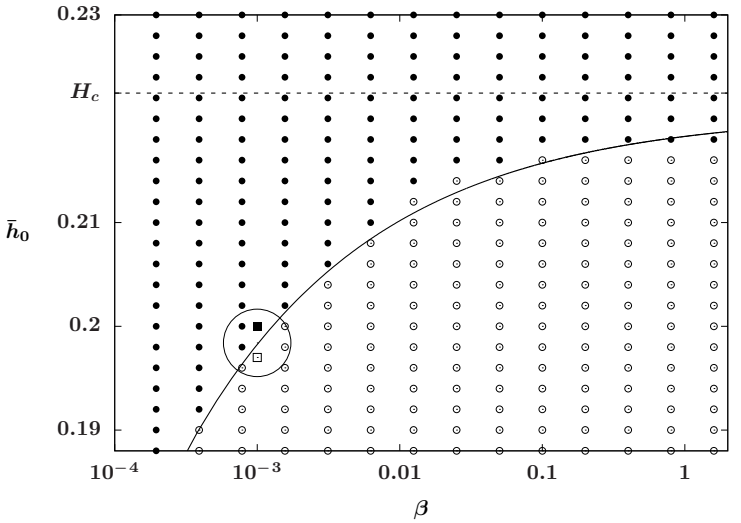

FIG. 21. Plot showing the influences of β and the initial film height to evaporation (denoted by open circles) or condensation (denoted by closed circles) dynamics. The $(\beta,\bar{h}_0)$ values used in Figs. 19 and 20 are labeled by closed and open squares, respectively.

VII. DISCUSSION

We have observed interesting transient pattern formation and interfacial instabilities of volatile thin fluid films from the model (1) in the weak evaporation limit. In a critical range of pressures, we have shown that transitions between filmwise and dropwise dynamics can yield various phase changes.

Unlike the conservative thin-film equation

$$\frac{\partial h}{\partial t} = \frac{\partial}{\partial x}\left(h^3 \frac{\partial}{\partial x}\left[\Pi(h) - \frac{\partial^2 h}{\partial x^2}\right]\right), \tag{41}$$

equivalent to $\beta = 0$ in (1), where a continuous family of nonuniform steady states with a constant pressure $p \equiv c$ exists in the system, the steady-state solutions of (1) correspond to a single value of the pressure determined by the liquid-vapor balance at the imposed temperature. While models for coarsening dynamics in (41) have been constructed [16], because of the difference in the set of steady states there are still open questions on how to formulate similar reduced models for volatile films.

While the focus of this paper has been on weak evaporative effects, we are also interested in transient patterns under strong evaporative influences (with β large). In particular, we would like to better understand the interaction between droplets coarsening and volatility and identify the behavior of the evaporation-condensation dividing line in Fig. 21 in the large-β limit.

In this paper the dynamics of a two-dimensional evaporative-condensing thin-film model has been demonstrated and we expect some of the results to be naturally extended to the three-dimensional case. Furthermore, the current nonlinear analysis of equilibrium stability is limited to a relatively small system. For a larger-scale domain more complicated and interesting pattern formation will arise and need further analysis.

We plan to further study the dynamics predicted by this mathematical model with parameter values appropriate to typical volatile fluids such as water or ethanol. Our assumption on Marangoni effects being negligible may put further constraints on ranges of parameters in the model. To test for robustness of the dynamics for pattern formation, we plan to include thermocapillary stresses and other physical effects such as vapor recoil and gravity in the model [30,36,37,57,58]. For instance,

in [59], destabilizing gravitation and stabilizing surface tension are considered for a film under a cooled horizontal plate. In [58], Panzarella *et al.* incorporated buoyancy, capillary, and evaporative effects to study a horizontal film boiling model.

APPENDIX: POSITIVITY OF SOLUTIONS WITH $\beta \geqslant 0$

In this Appendix we show that for $\beta \geqslant 0$ the evaporative mass flux cannot cause rupture singularities and the solution stays positive. The proof of this result depends on the properties of the disjoining pressure $\Pi(h)$ and the corresponding potential $U(h) = \int \Pi(h)dh$. From (2) we have $\lim_{h\to 0} U(h) = \infty$ and

$$\lim_{h\to\infty} U(h) = \begin{cases} -\infty & \text{for } P_0 > 0 \\ 0 & \text{for } P_0 = 0 \\ +\infty & \text{for } P_0 < 0, \end{cases}$$

where the borderline case is consistent with the properties of the potential function used in mass-conserving thin-film equations in [16,41]. The proof of this statement for $P_0 < 0$ is similar to the arguments from Ref. [41]. For $P_0 > 0$, we use an alternative approach to show the regularity of the solution.

Theorem. If $\beta \geqslant 0$ and the initial data satisfy $h_0 > 0$, $h_0 \in H^1([0,L])$, and $\mathcal{E}[h_0] < \infty$, then a unique positive smooth solution to Eq. (1) exists for all $t > 0$.

Proof. For $\beta \geqslant 0$ and $h > 0$, the functional (3) is monotonically dissipating. Using this fact, with the positive initial data, it suffices to derive *a priori* pointwise upper and lower bounds for the solution. Then the uniform parabolicity ensures that the solution is smooth and unique.

Since the functional is monotonically decreasing, at any time $T > 0$,

$$\frac{1}{2}\int_0^L \left|\frac{\partial h}{\partial x}(T)\right|^2 dx \leqslant \mathcal{E}[h_0] - \int_0^L U(h(T))dx. \tag{A1}$$

For $P_0 \leqslant 0$, we directly observe that $-U(h)$ has an *a priori* upper bound independent of h, implying that $\int |\partial_x h(x,T)|^2 dx$ is bounded. For $P_0 > 0$, while $-U(h) \to \infty$ as $h \to \infty$, based on the form of $U(h)$ in (2), we notice that $-U(h)$ has an upper bound

$$-U(h) = \left(\frac{\epsilon^2}{2h^2} - \frac{\epsilon^3}{3h^3}\right) + P_0 h \leqslant \frac{1}{6} + P_0 h. \tag{A2}$$

Then we consider the estimate for $\int |\partial_x h(x,T)|^2 dx$. Using the Cauchy-Schwarz inequality, one obtains that for any $0 \leqslant x$ and $y \leqslant L$,

$$|h(y) - h(x)| = \left|\int_x^y \partial_s h(s) ds\right| \leqslant \int_0^L |\partial_s h(s)| ds \leqslant L^{1/2}\left(\int_0^L |\partial_s h(s)|^2 ds\right)^{1/2}. \tag{A3}$$

Suppose that at time $t = T$ the solution $h(x,T)$ attains its minimum $h_{\min}$ at $x = x_0$. Then setting $y = x_0$ in (A3) yields

$$\int_0^L h(x,T)dx \leqslant \int_0^L |h_{\min} + [h(x,T) - h_{\min}]|dx \leqslant |h_{\min}|L + L^{3/2}\left(\int_0^L |\partial_x h(x,t)|^2 dx\right)^{1/2}. \tag{A4}$$

Using (A2) and (A4) we get

$$-\int_0^L U(h(T))dx \leqslant \frac{1}{6}L + P_0|h_{\min}|L + P_0 L^{3/2}\left(\int_0^L |\partial_x h(x,t)|^2 dx\right)^{1/2}. \tag{A5}$$

Combining (A5) and (A1) leads to

$$\tfrac{1}{2}\|\partial_x h(T)\|_{L^2}^2 - P_0 L^{3/2}\|\partial_x h(T)\|_{L^2} \leqslant \mathcal{E}[h_0] + \tfrac{1}{6}L + P_0|h_{\min}|L. \tag{A6}$$

Hence $h(x,T) \in H^1([0,L])$. Since the H^1-norm bounds the L^∞-norm in one space dimension, $h(x,T)$ has an *a priori* pointwise upper bound. Then we derive an *a priori* pointwise lower bound for $h(x,T)$. First, from (A1) we note that

$$\int_0^L U(h(x,T))dx < \mathcal{E}[h_0]. \tag{A7}$$

By the Sobolev embedding theorem, for some constant C_1 we have $\|h(x,T)\|_{C^{0,1/2}} \leqslant C_1\|h(x,T)\|_{H^1}$. Again suppose that $h(x,T)$ attains its minimum $h_{\min}$ at $x = x_0$. By the Hölder inequality, for some constant C_h we obtain $h(x) \leqslant h_{\min} + C_h|x - x_0|^{1/2}$. So for some constants $C_2(\epsilon) > 0$ and $C_3 > 0$, we have

$$\int_0^L U(h(x,T))dx \geqslant \int_0^L \frac{C_2(\epsilon)}{h(x,T)^3}dx - C_3 \geqslant \int_0^L \frac{C_2(\epsilon)}{(h_{\min} + C_h|x - x_0|^{1/2})^3}dx - C_3 \tag{A8}$$

and

$$\int_0^L \frac{C_2(\epsilon)}{(h_{\min} + C_h|x - x_0|^{1/2})^3}dx \geqslant \int_{x_0-(h_{\min}/C_h)^2}^{x_0+(h_{\min}/C_h)^2} \frac{C_2(\epsilon)}{(2h_{\min})^3}dx = \frac{C_2(\epsilon)}{4C_h^2 h_{\min}}. \tag{A9}$$

By (A7)–(A9), the solution cannot go below a positive threshold at any time $T > 0$. This completes our proof.

Remarks. When $\beta < 0$, the positivity of the solution is no longer guaranteed. Since the energy functional (3) is then not a Lyapunov functional, the energy argument presented in the proof does not apply to this case. In fact, finite-time rupture may occur and the PDE may break down past a critical time when specific values of system parameters are chosen (see [48]).

[1] A. Sharma and R. Khanna, Pattern Formation in Unstable Thin Liquid Films, Phys. Rev. Lett. **81**, 3463 (1998).

[2] E. M. Tian and D. J. Wollkind, A nonlinear stability analysis of pattern formation in thin liquid films, Interfaces Free Bound. **5**, 1 (2003).

[3] R. V. Craster and O. K. Matar, Dynamics and stability of thin liquid films, Rev. Mod. Phys. **81**, 1131 (2009).

[4] T. G. Myers, Thin films with high surface tension, SIAM Rev. **40**, 441 (1998).

[5] J. Ockendon, *Viscous Flow* (Cambridge University Press, Cambridge, 1995), Vol. 13.

[6] A. Oron, S. H. Davis, and S. G. Bankoff, Long-scale evolution of thin liquid films, Rev. Mod. Phys. **69**, 931 (1997).

[7] J. Becker, G. Grun, R. Seemann, H. Mantz, K. Jacobs, K. Mecke, and R. Blossey, Complex dewetting scenarios captured by thin-film models, Nat. Mater. **2**, 59 (2003).

[8] G. Reiter, Unstable thin polymer-films: Rupture and dewetting processes, Langmuir **9**, 1344 (1993).

[9] A. Sharma and G. Reiter, Instability of thin polymer films on coated substrates: Rupture, dewetting, and drop formation, J. Colloid Interface Sci. **178**, 383 (1996).

[10] M. B. Williams and S. H. Davis, Nonlinear theory of film rupture, J. Colloid Interface Sci. **90**, 220 (1982).

[11] T. P. Witelski and A. J. Bernoff, Dynamics of three-dimensional thin film rupture, Physica D **147**, 155 (2000).

[12] W. W. Zhang and J. R. Lister, Similarity solutions for van der Waals rupture of a thin film on a solid substrate, Phys. Fluids **11**, 2454 (1999).

[13] A. Ghatak, R. Khanna, and A. Sharma, Dynamics and morphology of holes in dewetting of thin films, J. Colloid Interface Sci. **212**, 483 (1999).

[14] J. R. King, A. Muench, and B. A. Wagner, Linear stability analysis of a sharp-interface model for dewetting thin films, J. Eng. Math. **63**, 177 (2009).

[15] A. Münch and B. Wagner, Impact of slippage on the morphology and stability of a dewetting rim, J. Phys.: Condens. Matter **23**, 184101 (2011).
[16] K. B. Glasner and T. P. Witelski, Coarsening dynamics of dewetting films, Phys. Rev. E **67**, 016302 (2003).
[17] V. S. Ajaev, J. Klentzman, T. Gambaryan-Roisman, and P. Stephan, Fingering instability of partially wetting evaporating liquids, J. Eng. Math. **73**, 31 (2012).
[18] U. Thiele, Thin film evolution equations from (evaporating) dewetting liquid layers to epitaxial growth, J. Phys.: Condens. Matter **22**, 084019 (2010).
[19] R. J. Braun, Dynamics of the tear film, Annu. Rev. Fluid Mech. **44**, 267 (2012).
[20] N. Miljkovic and E. N. Wang, Condensation heat transfer on superhydrophobic surfaces, MRS Bull. **38**, 397 (2013).
[21] P. L. Evans, L. W. Schwartz, and R. V. Roy, A mathematical model for crater defect formation in a drying paint layer, J. Colloid Interface Sci. **227**, 191 (2000).
[22] L. W. Schwartz, R. V. Roy, R. R. Eley, and S. Petrash, Dewetting patterns in a drying liquid film, J. Colloid Interface Sci. **234**, 363 (2001).
[23] J. W. Rose, Dropwise condensation theory and experiment: A review, Proc. Inst. Mech. Eng., Part A **216**, 115 (2002).
[24] R. Enright, N. Miljkovic, J. L. Alvarado, K. Kim, and J. W. Rose, Dropwise condensation on micro- and nanostructured surfaces, Nanoscale Microscale Thermophys. Eng. **18**, 223 (2014).
[25] K. Rykaczewski, A. T. Paxson, M. Staymates, M. L. Walker, X. Sun, S. Anand, S. Srinivasan, G. H. McKinley, J. Chinn, J. H. J. Scott, and K. K. Varanasi, Dropwise condensation of low surface tension fluids on omniphobic surfaces, Sci. Rep. **4**, 4158 (2014).
[26] R. Wen, Z. Lan, B. Peng, W. Xu, R. Yang, and X. Ma, Wetting transition of condensed droplets on nanostructured superhydrophobic surfaces: Coordination of surface properties and condensing conditions, ACS Appl. Mater. Interfaces **9**, 13770 (2017).
[27] R. Wen, Q. Li, J. Wu, G. Wu, W. Wang, Y. Chen, X. Ma, D. Zhao, and R. Yang, Hydrophobic copper nanowires for enhancing condensation heat transfer, Nano Energy **33**, 177 (2017).
[28] P. C. Wayner, Intermolecular forces in phase-change heat transfer: 1998 Kern award review, AIChE J. **45**, 2055 (1999).
[29] E. Sultan, A. Boudaoud, and M. Ben Amar, Evaporation of a thin film: Diffusion of the vapour and Marangoni instabilities, J. Fluid Mech. **543**, 183 (2005).
[30] J. P. Burelbach, S. G. Bankoff, and S. H. Davis, Nonlinear stability of evaporating/condensing liquid films, J. Fluid Mech. **195**, 463 (1988).
[31] A. Oron and S. G. Bankoff, Dewetting of a heated surface by an evaporating liquid film under conjoining/disjoining pressures, J. Colloid Interface Sci. **218**, 152 (1999).
[32] A. Oron and S. G. Bankoff, Dynamics of a condensing liquid film under conjoining/disjoining pressures, Phys. Fluids **13**, 1107 (2001).
[33] V. S. Ajaev, Evolution of dry patches in evaporating liquid films, Phys. Rev. E **72**, 031605 (2005).
[34] V. S. Ajaev, Spreading of thin volatile liquid droplets on uniformly heated surfaces, J. Fluid Mech. **528**, 279 (2005).
[35] V. S. Ajaev and G. M. Homsy, Steady vapor bubbles in rectangular microchannels, J. Colloid Interface Sci. **240**, 259 (2001).
[36] A. Amini and G. M. Homsy, Evaporation of liquid droplets on solid substrates. I. Flat substrate with pinned or moving contact line, Phys. Rev. Fluids **2**, 043603 (2017).
[37] A. Amini and G. M. Homsy, Evaporation of liquid droplets on solid substrates. II. Periodic substrates with moving contact lines, Phys. Rev. Fluids **2**, 043604 (2017).
[38] V. S. Ajaev and O. A. Kabov, Heat and mass transfer near contact lines on heated surfaces, Int. J. Heat Mass Transfer **108**, 918 (2017).
[39] A. Padmakar, K. Kargupta, and A. Sharma, Instability and dewetting of evaporating thin water films on partially and completely wettable substrates, J. Chem. Phys. **110**, 1735 (1999).
[40] A. Sharma, Equilibrium and dynamics of evaporating or condensing thin fluid domains: Thin film stability and heterogeneous nucleation, Langmuir **14**, 4915 (1998).

[41] A. L. Bertozzi, G. Grün, and T. P. Witelski, Dewetting films: Bifurcations and concentrations, Nonlinearity **14**, 1569 (2001).
[42] L. M. Hocking, The influence of intermolecular forces on thin fluid layers, Phys. Fluids A **5**, 793 (1993).
[43] D. M. Anderson and S. H. Davis, The spreading of volatile liquid droplets on heated surfaces, Phys. Fluids **7**, 248 (1995).
[44] D. Todorova, U. Thiele, and L. M. Pismen, The relation of steady evaporating drops fed by an influx and freely evaporating drops, J. Eng. Math. **73**, 17 (2012).
[45] J. Klentzman and V. S. Ajaev, The effect of evaporation on fingering instabilities, Phys. Fluids **21**, 122101 (2009).
[46] L. M. Pismen, Spinodal dewetting in a volatile liquid film, Phys. Rev. E **70**, 021601 (2004).
[47] B. Reisfeld, S. Bankoff, and S. Davis, The dynamics and stability of thin liquid films during spin coating. I. Films with constant rates of evaporation or absorption, J. Appl. Phys. **70**, 5258 (1991).
[48] H. Ji and T. P. Witelski, Finite-time thin film rupture driven by modified evaporative loss, Physica D **342**, 1 (2017).
[49] O. E. Shklyaev and E. Fried, Stability of an evaporating thin liquid film, J. Fluid Mech. **584**, 157 (2007).
[50] M. Cross and H. Greenside, *Pattern Formation and Dynamics in Nonequilibrium Systems* (Cambridge University Press, Cambridge, 2009).
[51] R. S. Laugesen and M. C. Pugh, Properties of steady states for thin film equations, Eur. J. Appl. Math. **11**, 293 (2000).
[52] R. S. Laugesen and M. C. Pugh, Energy levels of steady states for thin-film-type equations, J. Differ. Equations **182**, 377 (2002).
[53] R. S. Laugesen and M. C. Pugh, Linear stability of steady states for thin film and Cahn-Hilliard type equations, Arch. Ration. Mech. Anal. **154**, 3 (2000).
[54] R. Schaaf, Global behavior of solution branches for some Neumann problems depending on one or several parameters, J. Reine Angew. Math. **346**, 1 (1984).
[55] A. J. Bernoff, A. L. Bertozzi, and T. P. Witelski, Axisymmetric surface diffusion: Dynamics and stability of self-similar pinchoff, J. Stat. Phys. **93**, 725 (1998).
[56] K. Glasner and T. Witelski, Collision versus collapse of droplets in coarsening of dewetting thin films, Physica D **209**, 80 (2005).
[57] M. Bestehorn, A. Pototsky, and U. Thiele, 3D large scale Marangoni convection in liquid films, Eur. Phys. J. B **33**, 457 (2003).
[58] C. H. Panzarella, S. H. Davis, and S. G. Bankoff, Nonlinear dynamics in horizontal film boiling, J. Fluid Mech. **402**, 163 (2000).
[59] R. J. Deissler and A. Oron, Stable Localized Patterns in Thin Liquid Films, Phys. Rev. Lett. **68**, 2948 (1992).